Population Balance Modeling of Bubbly Flows Considering the Hydrodynamics and Thermomechanical Processes

Sherman C. P. Cheung
School of Aerospace, Mechanical and Manufacturing Engineering, RMIT University, Victoria 3083, Australia

G. H. Yeoh
Australian Nuclear Science and Technology Organisation (ANSTO), PMB 1, Menai, NSW 2234, Australia

J. Y. Tu
School of Aerospace, Mechanical and Manufacturing Engineering, RMIT University, Victoria 3083, Australia

DOI 10.1002/aic.11503
Published online April 18, 2008 in Wiley InterScience (www.interscience.wiley.com).

Three-dimensional two-fluid model and population balance equation is presented to treat the complex hydrodynamics and thermomechanical processes under various bubbly flow conditions. The class method, realized by the MUSIG model, alongside with suitable bubble coalescence and bubble breakage kernels is adopted. Homogeneous *MUSIG model predictions have shown to yield good agreement against isothermal bubbly flow measurements. Subcooled boiling flow is further modeled through the use of class method with an improved wall heat partition model. Against experimental data, numerical results also showed good agreement for the local Sauter mean bubble diameter, void fraction, and interfacial area concentration profiles. Inhomogeneous MUSIG model is applied to investigate transition bubbly-to-slug flow. Better prediction of bubble diameter is accomplished, especially capturing separation of small and large bubbles. Weakness exists nonetheless in the interfacial forces model. Work is in progress through the consideration of swarm and cluster bubbles instead of isolated spherical bubble calibration.* © 2008 American Institute of Chemical Engineers *AIChE J,* 54: 1689–1710, 2008
Keywords: population balance, bubbly flow, CFD, average bubble number density, bubble columns, bubble phenomena

Introduction

Complex gas–liquid bubbly flow structures are featured in many practical applications. Industrial systems that purposefully promote large interfacial areas for gas–liquid mass transfer and efficient mixing for competing gas–liquid reactions are extensively employed especially in the chemical, petroleum, mining and pharmaceutical industries. In the nuclear area, the ability to predict the void fraction distribution provides essential information toward assessments of safer reactor designs and operations. Such mounting industrial interests have certainly precipitated a number of significant experimental studies aiming to investigate and better understanding the heat and mass transfer and local hydrodynamics of bubbly flows.[1–4] Pertinent experimental observations have revealed clear tendencies of the bubbles within the bulk liquid flow to undergo deformation, coalescence, breakage and condensation within the particular system of interest

Correspondence concerning this article should be addressed to J. Tu at jiyuan.tu@rmit.edu.au.

subject to local flow conditions and heat and mass transfer processes.

From a modeling perspective, enormous challenges remain in fully resolving the many associated interfacial effects occurring between different phases subject to turbulence for a wide range of gas–liquid bubbly flows. Direct numerical simulation (DNS), which attempts to resolve the whole spectrum of possible turbulent length scales in the flow, can be adopted to possibly institute considerable insights into the complex morphologies that could persist within the two-phase flows. The phenomenal advancement of computer hardware and increasing computing power have certainly allowed the feasibility of using DNS in better studying individual bubble motions and its associated hydrodynamics behavior under modest turbulent flow conditions.[5,6] For highly turbulent flows such as experienced in actual industrial systems, DNS is still being greatly deterred from its full-blown engineering usage due to the constraints of computational resources. On the other hand, the population balance approach, which allows the evaluation of averaged bubble size distribution with appropriate considerations of the bubble behavior, is increasingly being adopted to handle such systems because of comparatively lower computational requirements in contrast to DNS. It is envisaged that the next stages of population balance modeling in research and in practice would most probably concentrate on the development of more definitive efficient algorithms for solving the population balance equation (PBE).

The foundation development of the PBE stems from the consideration of the Boltzman equation. Such equation is generally expressed in an *integrodifferential* form describing the particle size distribution (PSD). Owing to the complex phenomenological nature of particle dynamics, analytical solutions only exist for very simple cases.[7] In recent years, numerical approaches have been increasingly adopted to solve the PBE. The method of moment (MOM), first introduced by Hulburt and Katz,[8] has been considered as one of the many promising approaches in viably attaining practical solutions to the PBE. The basic idea behind MOM centers in the transformation of the problem into lower-order of moments of the size distribution, which are normally sufficient for estimating the physical quantities such as optical properties, volume fraction or Sauter mean diameter. Although MOM condenses the problem substantially by tracking the evolution of limited number of moments, the integrals that emerge during the process of transformation pose a serious closure problem[9] especially the involvement of the higher-order moments in the calculation. To overcome the closure problem, Frencklach[10] proposed a methodology whereby the required moments are determined via interpolative closure (MOMIC).

Another different approach for computing the moment is to approximate the integrals using numerical quadrature scheme—the quadrature method of moment (QMOM) as suggested by McGraw.[11] A number of approaches in the specific evaluation of the quadrature abscissas and weights have been proposed. McGraw[11] first introduced the product-difference (PD) algorithm formulated by Gordon[12] for solving monovariate problem. Later, McGraw and Wright[13] derived the Jacobian Matrix Transformation (JMT) for multi-component population. For multi-dimensional problems, Marchisio and Fox[14] extended the method by developing the "direct" QMOM where the quadrature abscissas and weights are formulated as transport equations; they are solved directly using matrix operations. Very recently, Grosch et al.[15] proposed a generalized framework for various QMOM approaches and evaluated different QMOM formulations in terms of numerical quadrature and dynamics simulation. Several studies have also been carried out validating the method against different gas–solid particle problems.[16–19] Encouraging results obtained thus far clearly demonstrated its usefulness in solving monovariate problems and its potential fusing within computational fluid dynamics (CFD) simulations. QMOM represents a rather sound mathematical approach and an elegant tool of solving the PBE with limited computational burden. Nonetheless, QMOM suffers some drawbacks in solving gas–liquid bubbly flows. As indicated in Marchisio and Fox,[20] instead of solving the PBE itself, tracking the moment through the transport equations introduces additional difficulties to treat systems where there is a strong dependency of the dispersed-phase velocity on the internal coordinates (i.e. bubbly flow system[21,22]). Marchisio and Fox[20] therefore proposed the "Direct" QMOM to circumvent this problem for moment method. Although a very clear derivation of the method was formulated, a thorough validation against bubbly experimental data was however outstanding. It can be concluded that the QMOM or other moment methods still require further assessments and validations for gas–liquid bubbly system.

Instead of inferring the PSD to derivative variables (i.e. moments), the class method (CM) which directly simulate its main characteristic using primitive variable (i.e. particle number density) has received greater attention due to its rather straightforward implementation within CFD software packages. Research studies based on the MUltiple-SIze-Group (MUSIG) model by Pochorecki et al.,[23] Olmos et al.,[24] Frank et al.,[25] Yeoh and Tu[26] and Cheung et al.[27] typified the application of CM in bubbly flow simulations. In the MUSIG model, the continuous size range of bubbles is discretized into a finite series of classes. By modeling the fundamental mechanisms of bubble coalescence and bubble breakage, population changes of each class and the overall PSD evolution are explicitly resolved as source terms within the transport equations. Sanyal et al.[28] examined and compared the CM and QMOM in a two-dimensional bubbly column simulation; both methods were found to yield very similar results. The CM solution was found to be independent of the resolution of the internal coordinate if sufficient number of classes was adopted. Unlike MOM, CM provides the feasibility of accounting different bubble shapes and traveling gas velocities. The inhomogeneous MUSIG model developed by Krepper et al.,[29] which consisted of sub-dividing the dispersed phase into N number of velocity fields, demonstrated the practicability of such an extension. This flexibility represents a robust feature for bubbly flows modeling. In spite of the sacrifices being made to computational efficiency, the extra computational effort will rapidly diminish due to foreseeable advancement of computer technology; the class method should therefore suffice as the preferred approach in tackling more complex bubbly flows.

For bubbly flows, the dynamic evolution of the PSD is governed predominantly by the bubble mechanistic behaviors such as bubble coalescence and bubble breakage. Figure 1a illustrates the physical characteristic of a typical isothermal bubbly flow. Owing to the positive lift force created by the lateral velocity gradient, small bubbles (under 5.5 mm for

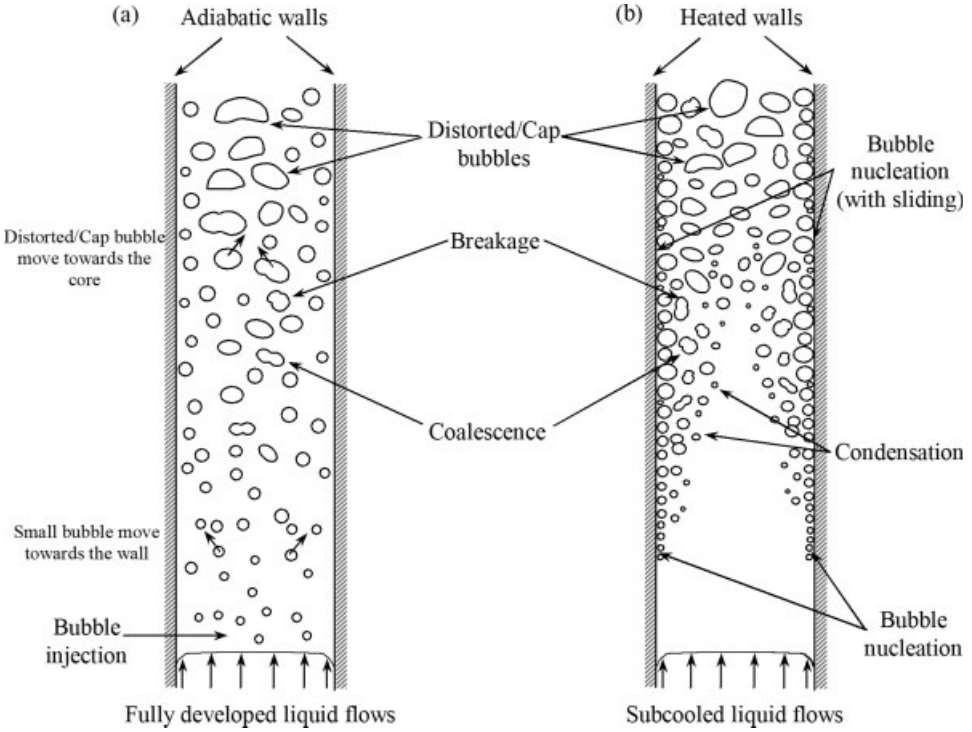

Figure 1. Schematic of the physical phenomenon embedded in (a) isothermal bubbly flows and (b) subcooled boiling flows.

air–water flows) being injected at the bottom have a tendency to migrate towards the channel walls thereby increasing the bubble number density near the wall region. The net effect of bubble coalescence encourages the formation of larger bubbles downstream. Larger bubbles (above 5.5 mm), driven by the negative lift force, will move toward to the centre core of the channel of which they will further coalesce with other bubbles to yield distorted/cap bubbles. These mechanisms strongly govern the distribution of bubble size and void fraction of the gas phase within the bulk liquid; appropriate sub-models (or kernels) in describing the bubble coalescence and bubble breakage are essential to the proper modeling of bubbly flows. The Prince and Blanch[30] coalescence and breakage kernels are widely applied for the CM approach. Various models focusing towards modifying the coalescence frequency and daughter bubble distribution due to breakage have also been proposed such as those from Chesters and Hoffman[31] Luo and Svendsen,[32] Lehr and Mewes,[33] Hagesaether et al.,[34] Wang et al.[35–37] and Andersson and Andersson.[38] Chen et al.[39] compared various kernels using a two-dimensional two-fluid model and showed that although the mechanistic considerations were different in each model, the predicted results were found to be rather similar across the broad range of models. A number of research studies have also been performed applying the aforementioned kernels to simulate size distribution evolution in bubbly turbulent pipe flows.[40–43] All these works were nonetheless limited in solving isothermal bubbly turbulent co-flow problems with low superficial gas velocity where there was no significant formation of cap/slug bubbles. It should be noted that the adoption of the above kernels remain debatable for modeling the bubble dynamics beyond bubbly flow regime, especially for high superficial gas velocity and flows involving complex inter-phase exchange of heat and mass transfer.

Subcooled boiling flow belongs to another special category of bubbly turbulent pipe flow which embraces the complex dynamic interactions of bubble coalescence and bubble breakage in the bulk flow as well as the presence of heat and mass transfer occurring in the vicinity of the heated wall due to nucleation and condensation. Heterogeneous bubble nucleation occurs naturally within small pits and cavities on the heated surface designated as nucleation sites as stipulated in Figure 1b, which is in contrast to having the bubbles being injected externally at the bottom of the flow as illustrated in Figure 1a for isothermal bubbly turbulent pipe flow. These nucleation sites, activated by external heat, act as a continuous source generating relatively small bubbles along the vertical wall of the channel. The presence of a heated wall represents the fundamental difference between isothermal bubbly and subcooled boiling flows, where the former has a constant bubble injection rate to govern the overall void fraction of gas phase, but the latter has a variable bubble nucleation rate which is subjected mainly to the heat transfer and phase changing phenomena. Furthermore, experimental observations have confirmed that the vapor bubbles, driven by external forces, have a tendency to travel a short distance away from the nucleation sites, gradually increasing in size, before lifting off into the bulk subcooled liquid.[44] Figure 2 shows a schematic illustration of the bubble motion and its area of influence on the heater surface. Such bubble motion not only alters the mode of heat transfer on the surface but

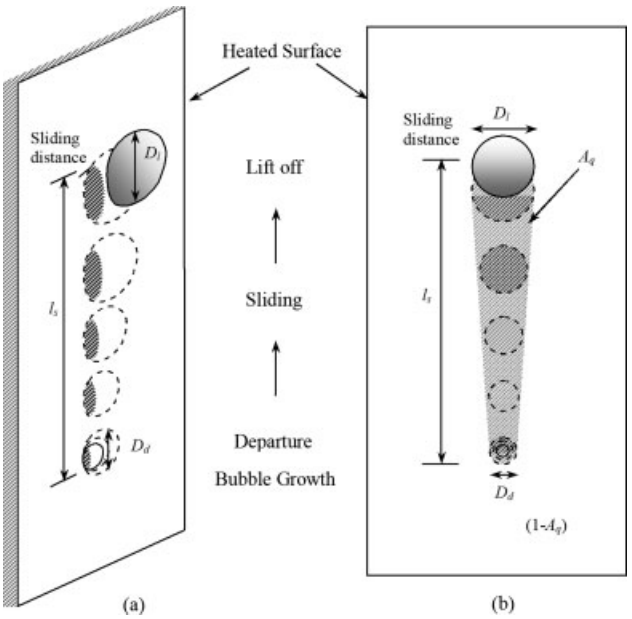

Figure 2. Schematic drawings illustrating (a) the mechanism of bubble departing, sliding and lifting off from a vertical heated surface and (b) the area of influence due to bubble growth and sliding referring to Eq. (29).

also governs the departure and lift-off diameter of bubbles, which in turn also influences the bubble distribution in the bulk liquid. In isothermal flow, coalescence prevails in the channel core where the turbulent dissipation rate is relatively low. Conversely, bubbles tend to decrease in size for subcooled boiling flow as a result of increasing condensation away from the heated walls since the temperature in the bulk liquid remains below the saturation temperature limit. This subcooling effect is a well-known phenomenon confirmed by various experiments.[45] Subject to this effect, such flows will certainly yield a broader range of bubble sizes and possibly even amplifying greater dynamical changes of the bubble size distribution when compared to isothermal bubbly turbulent pipe flow. Given the challenging task of modeling the sophisticated phenomena, empirical equations[46] were inevitably employed to determine the bubble diameter in the gas phase. To make progress, a modified version of the MUSIG model incorporating nucleation at the heated wall and condensation in the subcooled liquid were developed to better resolve the problem.[26,47] Although some empirical equations were still retained to determine the bubble nucleation and detachment, the potential of adopting population balance approach in subcooled boiling flow demonstrated considerable success in aptly predicting the bubble Sauter diameter distribution of the gas bubbles for vertical boiling flows.

In view of the current developments of the state-of-the-art, this article aims to further exploit the methodology of incorporating population balance approaches into the multiphase modeling using CFD techniques and the model's capability in handling practical gas–liquid bubbly flows with or without heat and mass transfer. Particular attention is given to CM as realized by the MUSIG model. Coupled with a three-dimensional two-fluid model alongside with suitable bubble coalescence and bubble breakage kernels, it is first assessed against isothermal bubbly turbulent pipe flow conditions. Results obtained from the *homogeneous* and *inhomogeneous* MUSIG models (to be further described below) are validated against local measurements of isothermal bubbly turbulent pipe flows in a vertical pipe performed by Hibiki et al.[48] Short-comings of existing interfacial force models in handling forces actuating on swarm and cluster bubbles which are prevalent in bubbly-to-slug transition flow condition and how the two models measure up in resolving the gas phase velocities are discussed. Bubble dynamics due to coalescence and breakage subject to the simultaneous occurrence of heat and mass transfer processes are also investigated. Predictions of the modified MUSIG model are compared against the experiment data of Yun et al.[49] and Lee et al.[50] for low-pressure subcooled boiling flows in annular channels. A closer examination on the evolution of gas bubble diameter in the bulk liquid is carried out by tracking the bubble size distribution along the radial direction. Some discussions and descriptions of an improved wall heat partition model[51] to better characterize the heat transfer and ebullition processes of the bubbles undergoing growth and subsequent detachment are also presented.

Mathematical Models

Two-fluid model

The three-dimensional two-fluid model solves the ensemble-averaged of mass, momentum and energy transport equations governing each phase. Denoting the liquid as the continuum phase (α_l) and the vapor (i.e. bubbles) as disperse phase (α_g), these equations can be written as:

Continuity equation of liquid phase

$$\frac{\partial \rho_l \alpha_l}{\partial t} + \nabla \cdot \left(\rho_l \alpha_l \vec{u}_l \right) = \Gamma_{lg} \tag{1}$$

Continuity equation of vapor phase

$$\frac{\partial \rho_g \alpha_g f_i}{\partial t} + \nabla \cdot \left(\rho_g \alpha_g f_i \vec{u}_g \right) = S_i - f_i \Gamma_{lg} \tag{2}$$

Momentum equation of liquid phase

$$\frac{\partial \rho_l \alpha_l \vec{u}_l}{\partial t} + \nabla . \left(\rho_l \alpha_l \vec{u}_l \vec{u}_l \right) = -\alpha_l \nabla P + \alpha_l \rho_l \vec{g} + \nabla \left[\alpha_l \mu_l^e \left(\nabla \vec{u}_l + \left(\nabla \vec{u}_l \right)^T \right) \right] + \left(\Gamma_{lg} \vec{u}_g - \Gamma_{gl} \vec{u}_l \right) + F_{lg} \tag{3}$$

Momentum equation of vapor phase

$$\frac{\partial \rho_g \alpha_g \vec{u}_g}{\partial t} + \nabla \cdot \left(\rho_g \alpha_g \vec{u}_g \vec{u}_g \right) = -\alpha_g \nabla P + \alpha_g \rho_g \vec{g} + \nabla \left[\alpha_g \mu_g^e \left(\nabla \vec{u}_g + \left(\nabla \vec{u}_g \right)^T \right) \right] + \left(\Gamma_{gl} \vec{u}_l - \Gamma_{lg} \vec{u}_g \right) + F_{gl} \tag{4}$$

Energy equation of liquid phase

$$\frac{\partial \rho_l \alpha_l H_l}{\partial t} + \nabla \cdot \left(\rho_l \alpha_l \vec{u}_l H_l \right) = \nabla \left[\alpha_l \lambda_l^e (\nabla T_l) \right] + \left(\Gamma_{gl} H_l - \Gamma_{lg} H_g \right) \tag{5}$$

Energy equation of vapor phase

$$\frac{\partial \rho_g \alpha_g H_g}{\partial t} + \nabla \cdot \left(\rho_g \alpha_g \vec{u}_g H_g\right) = \nabla\left[\alpha_g \lambda_g^e \left(\nabla T_g\right)\right] + \left(\Gamma_{gl} H_l - \Gamma_{lg} H_g\right) \quad (6)$$

On the right-hand side of Eq. 2, S_i represents the additional source terms due to coalescence and breakage. For isothermal bubbly turbulent pipe flows, it should be noted that the mass transfer rate Γ_{lg} and Γ_{gl} are essentially 0. The total interfacial force F_{lg} appearing in Eq. 3 is formulated according to appropriate consideration of different sub-forces affecting the interface between each phase. For the liquid phase, the total interfacial force is given by:

$$F_{lg} = F_{lg}^{drag} + F_{lg}^{lift} + F_{lg}^{lubrication} + F_{lg}^{dispersion} \quad (7)$$

The sub-forces appearing on the right hand side of Eq 7 are: drag force, lift force, wall lubrication force and turbulent dispersion force. More detail descriptions of these sub-forces can be found in Anglart and Nylund.[46] Note that for the gas phase, $F_{gl} = -F_{lg}$.

The interfacial mass transfer rate due to condensation in the bulk subcooled liquid in Eq. 2 can be expressed by:

$$\Gamma_{lg} = \frac{h a_{if} (T_{sat} - T_l)}{h_{fg}} \quad (8)$$

Here, h indicates the inter-phase heat transfer coefficient which is correlated in terms of the Nusselt number.[52] The wall generation rate for the vapor is modeled in a mechanistic manner by considering the total mass of bubbles detaching from the heated surface as:

$$\Gamma_{gl} = \frac{Q_e}{h_{fg} + C_{pl}(T_{sat} - T_l)} \quad (9)$$

Here, Q_e refers as the heat transfer rate due to evaporation. For subcooled boiling flows, the wall nucleation rate is accounted in Eq. 2 as a specified boundary condition apportioned to the discrete bubble class based on the size of the bubble lift-off diameter, which is evaluated from the improved wall heat partition model. The term $f_i \Gamma_{lg}$ represents the mass transfer due to condensation. The gas void fraction along with the scalar size fraction f_i are related to the number density of the discrete bubble ith class n_i (similar to the jth class n_j) as $\alpha_g f_i = n_i v_i$.

Turbulence Modeling for Two-fluid Model. For the liquid phase, the Shear Stress Transport (SST) model[53] is adopted in the present study. The SST model is a hybrid version of the k–ε and k–ω models with a specific blending function. Instead of using empirical wall function to bridge the wall and the far-away turbulent flow, it solves the two turbulence scalars (i.e. k and ω) explicitly down to the wall boundary. The ensemble-averaged transport equations of the SST model are given as:

$$\frac{\partial \rho_l \alpha_l k_l}{\partial t} + \nabla \cdot \left(\rho_l \alpha_l \vec{u}_l k_l\right) = \nabla \cdot \left(\alpha_l \left(\mu_l + \frac{\mu_{t,l}}{\sigma_{k3}}\right) \nabla k_l\right) + \alpha_l P_{k,l} - \rho_l \beta' k_l \omega_l$$

$$\frac{\partial \rho_l \alpha_l \omega_l}{\partial t} + \nabla \cdot \left(\rho_l \alpha_l \vec{u}_l \omega_l\right) = \nabla \cdot \left(\alpha_l \left(\mu_l + \frac{\mu_{t,l}}{\sigma_{\omega 3}}\right) \nabla \omega_l\right) - 2\rho_l \alpha_l (1 - F_1) \frac{1}{\sigma_{\omega 2} \omega_l} \frac{\partial k_l}{\partial x_j} \frac{\partial \omega_l}{\partial x_j} + \alpha_l \gamma_3 \frac{\omega_l}{k_l} P_{k,l} - \rho_l \beta_3 \omega_l^2 \quad (10)$$

where σ_{k3}, $\sigma_{\omega 3}$, γ_3, and β_3 are the model constants which are evaluated based on the blending function F_1. The shear induced turbulent viscosity $\mu_{ts,l}$ is given by:

$$\mu_{ts,l} = \frac{\rho a_1 k_l}{\max(a_1 \omega_l, S F_2)}, \quad S = \sqrt{2 S_{ij} S_{ij}} \quad (11)$$

The success of SST model hinges on the use of blending functions of F_1 and F_2 which govern the crossover point between the k–ω and k–ε models. The blending functions are given by:

$$F_1 = \tan h\left(\Phi_1^4\right), \quad \Phi_1 = \min\left[\max\left(\frac{\sqrt{k_l}}{0.09 \omega_l d_n}, \frac{500 \mu_l}{\rho_l \omega_l d_n^2}\right), \frac{4 \rho_l k_l}{D_\omega^+ \sigma_{\omega 2} d_n^2}\right] \quad F_2 = \tan h\left(\Phi_2^2\right), \quad \Phi_2 = \max\left(\frac{\sqrt{k_l}}{0.09 \omega_l d_n}, \frac{500 \mu_l}{\rho_l \omega_l d_n^2}\right) \quad (12)$$

Here, default values of model constants were adopted. More detail descriptions of these model constants can be found in Menter.[53] In addition, to account the effect of bubbles on liquid turbulence, the Sato's bubble-induced turbulent viscosity model[54] was also employed. The turbulent viscosity of liquid phase is therefore given by:

$$\mu_{t,l} = \mu_{ts,l} + \mu_{td,l} \quad (13)$$

and the particle induced turbulence can be expressed as:

$$\mu_{td,l} = C_{\mu p} \rho_l \alpha_g D_s |\vec{U}_g - \vec{U}_l| \quad (14)$$

For the gas phase, dispersed phase zero equation model was adopted and the turbulent viscosity of gas phase can be obtained as:

$$\mu_{t,g} = \frac{\rho_g}{\rho_l} \frac{\mu_{t,l}}{\sigma_g} \quad (15)$$

where σ_g is the turbulent Prandtl number of the gas phase.

MUSIG models

The Homogeneous and Inhomogeneous MUSIG Models. In this study, the CM as realized through the MUSIG model is adopted to account for the non-uniform bubble size distribution in bubbly and subcooled boiling flows. Figure 3 shows the discrete bubble classes employed to characterize the two different flows.

The *homogeneous* MUSIG model developed by Lo[55] is implemented as an additional feature within the generic CFD computer code CFX-4.4. Within the model, the continuous bubble size distribution (BSD) function is approximated by

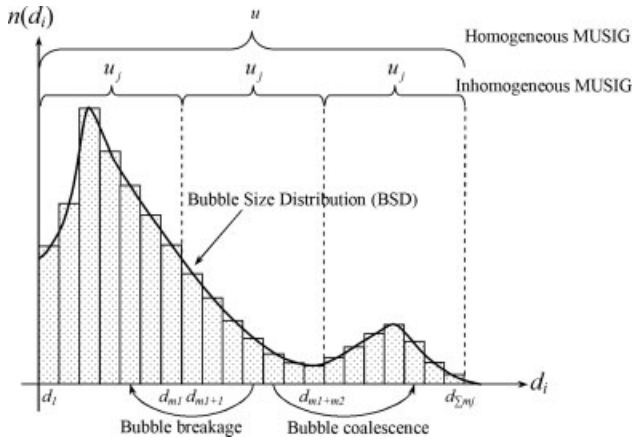

Figure 3. Graphical presentations of the homogeneous and inhomogeneous MUSIG models.

M number size fractions; the mass conversation of each size fractions are balanced by the inter-fraction mass transfer due to the bubble coalescence and bubble breakage processes. For computational efficiency, the model assumes that all size fractions are taken to travel with the same velocity field. As elucidated in Figure 1a, this assumption imposes a restriction to account for a broad range of bubble sizes that may be traveling with different slip velocities. Recently, Krepper et al.[29] proposed an *inhomogeneous* MUSIG model which further divides the gaseous dispersed phase into N number of velocity groups. It should be noted that conservation of mass is still ensured between the size fractions of dispersed phase across different velocity groups. Useful information on the implementation and application of the *inhomogeneous* MUSIG model can be found in Shi et al.[56] and Krepper et al.[57]

The formulation of the MUSIG model originates from the discretized PSE, which can be expressed in terms of discrete bubble number density as:

$$\frac{\partial n_i}{\partial t} + \nabla \cdot \left(\vec{u}_i n_i\right) = \left(\sum R\right)_i - \left(R_{\mathrm{ph}}\right)_i \tag{16}$$

To ensure overall mass conservation for all poly-dispersed vapor phases, the above bubble number density equation for the *inhomogeneous* MUSIG model can be re-expressed in terms of the volume fraction and size fraction of the bubble size class i, $i \in [1,M_j]$, of velocity group j,$j \in [1,N]$ according to:

$$\frac{\partial \rho_j \alpha_j f_i}{\partial t} + \nabla \cdot \left(\rho_{\mathrm{g}} \alpha_j f_i \vec{u}_j\right) = S_{j,i} - m_i \left(R_{\mathrm{ph}}\right)_i \tag{17}$$

with additional relations and constraints:

$$\begin{aligned} &\alpha_{\mathrm{g}} = \sum_{j=1}^{N} \alpha_j = \sum_{j=1}^{N} \sum_{i=1}^{M_j} \alpha_{ij}; \qquad \alpha_j = \sum_{i=1}^{M_j} \alpha_i \\ &\alpha_{\mathrm{g}} + \alpha_{\mathrm{l}} = 1; \quad \sum_{i=1}^{M_j} f_i = 1 \end{aligned} \tag{18}$$

where m_{i} is the mass fraction of the bubble size group i.

On the right-hand side of Eq. 17, the term $S_{j,i} = m_i(\sum R)_i = (P_{\mathrm{C}} + P_{\mathrm{B}} - D_{\mathrm{C}} - D_{\mathrm{B}})$ represents the net mass transfer rate of the bubble class i resulting from the source of P_{C}, P_{B}, D_{C}, and D_{B}, which are the production rates due to coalescence and breakage and the death rate due to coalescence and breakage of bubbles, respectively. They can be formulated as:

$$\begin{aligned} P_{\mathrm{C}} &= \frac{1}{2} \sum_{k=1}^{i} \sum_{\mathrm{l}=1}^{i} \eta_{jki} \chi_{ij} n_i n_j \\ \eta_{jki} &= \begin{cases} \left(v_j + v_k\right) - v_{i-1} / (v_i - v_{i-l}) & \text{if } v_{i-1} < v_j + v_k < v_i \\ v_{i+1} - \left(v_j + v_k\right) / (v_{i+1} - v_i) & \text{if } v_i < v_j + v_k < v_{i+1} \\ 0 & \text{otherwise} \end{cases} \\ D_{\mathrm{C}} &= \sum_{j=1}^{N} \chi_{ij} n_i n_j \\ P_{\mathrm{B}} &= \sum_{j=i+1}^{N} \Omega\left(v_j : v_i\right) n_j \\ D_{\mathrm{B}} &= \Omega_i n_i \quad \text{with} \quad \Omega_i = \sum_{k=1}^{N} \Omega_{ki} \end{aligned} \tag{19}$$

with

$$S_j = \sum_{i=1}^{M_j} S_{j,i} \quad \text{and} \quad \sum_{j=1}^{N} S_j = 0 \tag{20}$$

Bubble Coalescence and Breakage Kernels. Bubble breakage rate of volume v_j into volume v_i is modeled according to Luo and Svendsen,[32] which is based on the assumption of bubble binary breakage under isotropic turbulence situation. The daughter size distribution is accounted using a stochastic breakage volume fraction f_{BV}. Denoting the increase coefficient of surface area as $c_f = [f_{\mathrm{BV}}^{2/3} + (1 - f_{\mathrm{BV}})^{2/3} - 1]$, the breakage rate can be obtained as:

$$\begin{aligned} \frac{\Omega\left(v_j : v_i\right)}{\left(1 - \alpha_{\mathrm{g}}\right) n_j} &= F_{\mathrm{B}} C \left(\frac{\varepsilon}{d_j^2}\right)^{1/3} \\ &\times \int_{\xi_{\min}}^{1} \frac{(1+\xi)^2}{\xi^{11/3}} \times \exp\left(-\frac{12 c_f \sigma}{\beta \rho_{\mathrm{l}} \varepsilon^{2/3} d^{5/3} \xi^{11/3}}\right) d\xi \end{aligned} \tag{21}$$

where $\xi = \lambda / d_j$ is the size ratio between an eddy and a particle in the inertial sub-range and consequently $\xi_{\min} = \lambda_{\min} / d_j$ and C and β are determined from fundamental consideration of drops or bubbles breakage in turbulent dispersion systems to be 0.923 and 2.0. F_{B} is the breakage calibration factor.

Bubble coalescence occurs via collision of two bubbles which may be caused by wake entrainment, turbulence random collision and buoyancy. Only turbulence random collision is considered in the present study as all bubbles are assumed to be of spherical shape (wake entrainment becomes negligible). The coalescence rate considering the turbulent collision taken from Prince and Blanch[30] can be expressed as:

$$\chi_{ij} = F_{\mathrm{C}} \frac{\pi}{4} \left[d_i + d_j\right]^2 \left(u_{ti}^2 + u_{tj}^2\right)^{0.5} \exp\left(-\frac{t_{ij}}{\tau_{ij}}\right) \tag{22}$$

where τ_{ij} is the contact time for two bubbles given by $(d_{ij}/2)^{2/3} / \varepsilon^{1/3}$ and t_{ij} is the time required for two bubbles to coalesce

having diameter d_i and d_j estimated to be $[(d_{ij}/2)^3\ \rho_l/16\sigma]^{0.5}\ \ln(h_0/h_f)$. The equivalent diameter d_{ij} is calculated as suggested by Chesters and Hoffman[31]: $(d_{ij} = (2/d_i + 2/d_j)^{-1}$. According to Prince and Blanch,[30] experiments have determined the initial film thickness $h_0 = 1 \times 10^{-4}$ m and critical film thickness $h_f = 1 \times 10^{-8}$ m at which rupture for air–water systems. The turbulent velocity u_t in the inertial sub-range of isotropic turbulence[58] which is given by: $u_r = \sqrt{2}\varepsilon^{1/3}d^{1/3}$. F_C is the coalescence calibration factor.

Bubble Source and Sink due to Phase Change in Subcooled Boiling Flows. The term $(R_{ph})_i$ in Eq. 16 constitutes the essential formulation of the source/sink rate for the phase change processes associated with subcooled boiling flow. Considering the condensation of bubbles, the bubble condensation rate in a control volume for each bubble class can be determined from:

$$\phi_{COND} = -\frac{n_i}{V_B}A_B\frac{dR}{dt} \tag{23}$$

The bubble condensation velocity[45] is obtained from:

$$\frac{dR}{dt} = \frac{h(T_{sat} - T_l)}{\rho_g h_{fg}} \tag{24}$$

Substituting Eq. 24 into Eq. 23, and given that the bubble surface are A_B and volume V_B which are based on Sauter mean bubble diameter, Eq. 23 can be rearranged to yield:

$$(R_{ph})_i = \phi_{COND} = -\frac{1}{\rho_g \alpha_i}\left[\frac{ha_{if}(T_{sat} - T_l)}{h_{fg}}\right]n_i \tag{25}$$

At the heated surface, bubbles at the nucleation sites are formed through the evaporation processes. The bubble nucleation rate from these sites can be expressed as:

$$\phi_{WN} = \frac{Naf\xi_H}{A_C} \tag{26}$$

where Na, f, ξ_H and A_C is the active nucleation site density, the bubble generation frequency from the nucleation sites, the heated perimeter, and the cross-sectional area of the boiling channel, respectively. Because the bubble nucleation process is taken to occur only at the heated surface, this heated wall nucleation rate is treated as a specified boundary condition to Eq. 16, apportioned to the discrete bubble class i, based on the bubble lift-off diameter determined from the mechanistic wall heat partition model.

Mechanistic wall heat partition model

To determine the bubble generation frequency and lift-off diameter for the boundary condition of the MUSIG model, an improved wall heat partition model based on a mechanistic approach is proposed[51] and briefly discussed in this section. With the presence of convective force or buoyancy force acting upon a vertically orientated boiling flow as depicted in Figure 2a, vapor bubble departs from its nucleation site, slides along the heating surface and continues to grow downstream until it lifts off from the surface.[44] The motion of the traveling bubble affects the heat transfer at the heated wall according to two mechanisms: (i) the latent heat transfer due to micro-layer evaporation and (ii) transient conduction as the disrupted thermal boundary layer reforms during the waiting period (i.e. incipience of the next bubble at the same nucleation site).

Transient Conduction due to Bubble Motion. Transient conduction occurs in regions at the point of inception and in regions being swept by sliding bubbles. For a stationary bubble, the heat flux is given by:

$$Q_{tc} = 2\sqrt{\frac{k_l\rho_l C_{pl}}{\pi t_w}}(T_s - T_l)R_f N_a\left(K\frac{\pi D_d^2}{4}\right)t_w f + 2\sqrt{\frac{k_l\rho_l C_{pl}}{\pi t_w}}(T_s - T_l)R_f N_a\left(\frac{\pi D_d^2}{4}\right)(1 - t_w f) \tag{27}$$

where D_d is the bubble departure diameter, T_s is the temperature of the heater surface and T_l is the temperature of the liquid. Eq. 27 indicates that some fraction of the nucleation sites will undergo transient conduction whereas the remaining will be in the growth period. For a sliding bubble, the heat flux due to transient conduction that takes place during the sliding phase and the area occupied by the sliding bubble at any instant of time is given by:

$$Q_{tcsl} = 2\sqrt{\frac{k_l\rho_l C_{pl}}{\pi t_w}}(T_s - T_l)R_f N_a l_s K D t_w f + 2\sqrt{\frac{k_l\rho_l C_{pl}}{\pi t_w}}(T_s - T_l)R_f N_a f t_{sl}\left(\frac{\pi D^2}{4}\right)(1 - t_w f) \tag{28}$$

where the average bubble diameter D is given by $D = (D_d + D_l)/2$ and D_l is the bubble lift-off diameter. In this study, a value of 1.8 is assumed for the area of influence, K.[59] The reduction factor R_f appearing in Eqs. 27 and 28 depicts the ratio of the actual number of bubbles lifting off per unit area of the heater surface to the number of active nucleation sites per unit area, viz., $R_f = 1/(l_s/s)$ where l_s is the sliding distance and s is the spacing between nucleation sites. In the present study, the spacing between nucleation sites is approximated as $s = 1/\sqrt{N_a}$.[60] The active nucleation site density, N_a, is expressed by $N_a = [185(T_w - T_{sat})]^{1.805}$.[61] The factor R_f is obtained alongside with the sliding distance evaluated from the force balance model described below.

Force Convection for Single Phase Component. Forced convection always prevails at all times in areas of the heater surface that are not influenced by the stationary and sliding bubbles (see also in Figure 2b). The fraction of the heater area for stationary and sliding bubbles is given by:

$$1 - A_q = 1 - R_f\left[N_a\left(K\frac{\pi D_d^2}{4}\right)t_w f + N_a\left(\frac{\pi D_d^2}{4}\right)(1 - t_w f) + N_a l_s K D t_w f + N_a f t_{sl}\left(\frac{\pi D_d^2}{4}\right)(1 - t_w f)\right] \tag{29}$$

The heat flux due to forced convection can be obtained according to the definition of local Stanton number St for turbulent convection is:

$$Q_c = St\rho_l C_{pl} u_l (1 - A_q)(T_w - T_l) \tag{30}$$

where u_l is the adjacent liquid velocity.

Latent Heat due to Vapor Evaporation Processes. The heat flux attributed to vapor generation is given by the energy carried away by the bubbles lifting off from the heated surface. It also represents the energy of vaporization whereby the bubble size of D_l is produced, which is expressed as:

$$Q_e = R_f N_a f \left(\frac{\pi D_l^3}{6}\right) \rho_g h_{fg} \tag{31}$$

The total wall heat flux Q_w is the combination of the following heat flux components: $Q_w = Q_e + Q_{tc} + Q_{tcsl} + Q_c$.

Mechanistic Approach for Bubble Frequency Evaluation. The bubble nucleation rate in Eq. 26 requires the knowledge of the bubble frequency (f). Within the wall partition model, the bubble frequency is determined by a mechanistic approach based on the description of an ebullition cycle in nucleate boiling, which is formulated as:

$$f = \frac{1}{t_g + t_w} \tag{32}$$

The waiting period (t_w) and the growth period of vapor bubbles (t_g) is derived from the transient conduction and force balance model, respectively.

When transient conduction occurs, the boundary layer gets disrupted and cold liquid comes in contact with the heated wall. Assuming that the heat capacity of the heater wall $\rho_s C_{ps} \delta_s$ is very small, the conduction process can be modeled by considering one-dimensional transient heat conduction into a semi-infinite medium with the liquid at a temperature T_l and the heater surface at a temperature T_s. The wall heat flux can be approximated by:

$$Q_w = \frac{k_l (T_s - T_l)}{\delta_l} \tag{33}$$

where $\delta_l (= \sqrt{\pi \eta t})$ is the thickness of the thermal boundary layer. If the temperature profile inside this layer is taken to be linear,[62] it can be expressed as:

$$T_b = T_w - \frac{(T_s - T_l)x}{\delta_l} \tag{34}$$

where x is the normal distance from the wall. Based on the criterion of the incipience of boiling from a bubble site inside the thermal boundary layer, the bubble internal temperature for a nucleus site (cavity) with radius r_c is

$$T_b = T_{sat} - \frac{2\sigma T_{sat}}{C_2 r_c h_{fg} \rho_g} \quad \text{at} \quad x = C_1 r_c \tag{35}$$

where $C_1 = (1 + \cos\theta)/\sin\theta$ and $C_2 = 1/\sin\theta$. The angle θ represents the bubble contact angle. By substituting Eq. 35 into Eq. 34, the waiting time t_w can be obtained as

$$t = t_w = \frac{1}{\pi \eta} \left[\frac{(T_s - T_l) C_1 r_c}{(T_w - T_{sat}) - 2\sigma T_{sat}/C_2 \rho_g h_{fg} r_c}\right]^2 \tag{36}$$

The cavity radius r_c can be determined by applying Hsu's criteria and tangency condition of Eqs. 9 and 10, viz.,

$$t = \left[\frac{C_1 C_2 \rho_g h_{fg} r_c^2}{2\sigma T_{sat}}\right]^2 \frac{(T_s - T_l)^2}{\pi \eta} = \left[\frac{k_l}{Q_w}\right]^2 \frac{(T_s - T_l)^2}{\pi \eta} \tag{37}$$

From the above equation,

$$r_c = F \left[\frac{2\sigma T_{sat} k_l}{\rho_g h_{fg} Q_w}\right]^{1/2} \tag{38}$$

where,

$$F = \left(\frac{1}{C_1 C_2}\right)^{1/2} = \left(\frac{\sin^2\theta}{1 + \cos\theta}\right)^{1/2} \tag{39}$$

According to Basu et al.,[60] the factor F indicates the degree of flooding of the available cavity size and the wettability of the surface. If the contact angle $\theta \to 0$, all the cavities will be flooded. Alternatively, as $\theta \to 90^\circ$, $F \to 1$, all the cavities will not be flooded (i.e. they contain traces of gas or vapor).

Force Balance Model and the Bubble Growth Time. The bubble growth time is correlated to its lift-off diameter which depends on various forces acting on the bubble in the directions parallel and normal to a vertical heating surface. Figure 4 illustrates the forces acting on the bubble in the x-direction and y-direction which can be formulated according to the studies performed by Klausner et al.[44] and Zeng et al.[63]:

$$\Sigma F_x = F_{sx} + F_{dux} + F_{sL} + F_h + F_{cp} \tag{40}$$

and

$$\Sigma F y = F_{sy} + F_{duy} + F_{qs} + F_b \tag{41}$$

where F_s is the surface tension force, F_{du} is the unsteady drag due to asymmetrical growth of the bubble and the dynamic effect of the unsteady liquid such as the history force and the added mass force, F_{sL} is the shear lift force, F_h is the force due to the hydrodynamic pressure, F_{cp} is the contact pressure force accounting for the bubble being in contact with a solid rather than being surrounded by liquid, F_{qs} is the quasi steady-drag in the flow direction, and F_b is the buoyancy force. In addition, g indicates the gravitational acceleration; α, β, and θ_i are the advancing, receding and inclination angles respectively; d_w is the surface/bubble contact diameter; and d is the vapor bubble diameter at the wall.

The forces acting in the x-direction can be estimated from:

$$\begin{aligned} &F_{sx} = -d_w \sigma \frac{\pi}{\alpha - \beta}[\cos\beta - \cos\alpha]; \quad F_{dux} = -F_{du} \cos\theta \\ &F_{sL} = \frac{1}{2} C_L \rho_l \Delta U^2 \pi r^2; \quad F_h = \frac{9}{4} \rho_l \Delta U^2 \frac{\pi d_w^2}{4} \\ &F_{cp} = \frac{\pi d_w^2}{4} - \frac{2\sigma}{r_r} \end{aligned} \tag{42}$$

The forces acting in the x-direction can be estimated from:

$$\begin{aligned} &F_{sy} = -d_w \sigma \frac{\pi(\alpha - \beta)}{\pi^2 - (\alpha - \beta)^2}[\sin\alpha + \sin\beta]; \quad F_{duy} = -F_{du} \sin\theta \\ &F_{qs} = 6 C_D \mu_l \Delta U \pi r; \quad F_b = \frac{4}{3} \pi r^3 (\rho_l - \rho_g) g \end{aligned} \tag{43}$$

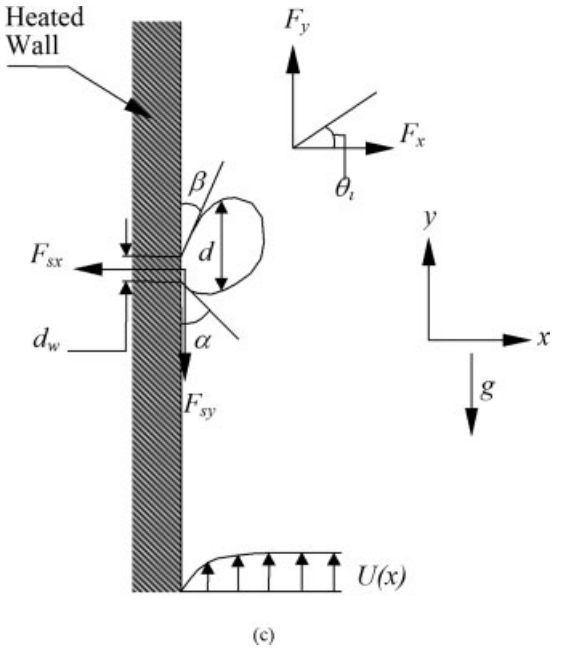

Figure 4. Schematic drawings illustrating the forces balance of a growing vapor bubble attached to the heated surface.

From the various forces described along the x-direction and y-direction, r is the bubble radius, ΔU is the relative velocity between the bubble center of mass and liquid, C_D and C_L are the respective drag and shear lift coefficients and r_r is the curvature radius of the bubble at the reference point on the surface $x = 0$, which is $r_r \sim 5r$.[44]

The growth force F_{du} is modeled by considering a hemispherical bubble expanding in an inviscid liquid, which is given by Zeng et al.[63] as:

$$F_{du} = \rho_l \pi r^2 \left(\frac{3}{2} C_s \dot{r}^2 + r\ddot{r} \right) \tag{44}$$

where $(\dot{})$ indicates differentiation with respect to time. The constant C_s is taken to be 20/3.[63] In estimating the growth force, additional information on the bubble growth rate is required. As in Zeng et al.,[63] a diffusion controlled bubble growth solution by Zuber[64] is adopted:

$$r(t) = \frac{2b}{\sqrt{\pi}} Ja \sqrt{\eta t}; \quad Ja = \frac{\rho_l C_{pl} \Delta T_{sat}}{\rho_g h_{fg}}; \quad \eta = \frac{k_l}{\rho_l C_{pl}} \tag{45}$$

where Ja is the Jakob number, η is the liquid thermal diffusivity and b is an empirical constant that is intended to account for the asphericity of the bubble. For the range of heat fluxes investigated in this investigation, b is taken to be 0.21 based on a similar subcooled boiling study performed by Steiner et al.,[65] which has been experimentally verified through their in-house measurements with water as the working fluid.

Although a vapor bubble remains attached to the heated wall, the sum of the parallel and normal forces must satisfy the following conditions: $\Sigma F_x = 0$ and $\Sigma F_y = 0$. For a sliding bubble case, the former establishes the bubble departure diameter (D_d) whereas the latter yields the bubble lift-off diameter (D_l). The growth period t_g appearing in Eq. 32 can be readily evaluated based on the availability of the bubble size at departure from its nucleation site through Eq. 45. Details of the present wall partition model can also be found in literature[51] and the references therein.

Experimental Details

Brief discussions of the experimental setup for the isothermal and subcooled bubbly turbulent pipe flows are provided below.

Isothermal bubbly turbulent pipe flow experiments have been performed at the Thermal-Hydraulics and Reactor Safety Laboratory in Purdue University.[48] The test section comprised of an acrylic round pipe with an inner diameter $D = 50.8$ mm and a length of 3061 mm. Temperature of the apparatus was kept at a constant temperature (i.e. 20°C) within a deviation of ±0.2°C controlled by a heat exchanger installed in a water reservoir. Local flow measurements using the double sensor and hotfilm anemometer probes were performed at three axial (height) locations of $z/D = 6.0$, 30.3, and 53.5 and 15 radial locations of $r/R = 0$ to 0.95. Experiments at a range of superficial liquid velocities j_f and superficial gas velocities j_g were performed covering most bubbly flow regions including finely dispersed bubbly flow and bubbly-to-slug transition flow regions.

A series of subcooled boiling experiments have been performed by Yun et al.[49] and Lee et al.[50] The experimental setup consisted of a vertical concentric annulus with an inner rod of 19 mm outer diameter uniformly heated by a 54 kW DC power supply. This heated section comprised of a 1.67 m long Inconel 625 tube with a 1.5 mm wall thickness filled with magnesium oxide powder insulation. The outer wall comprised of two stainless steel tubes with 37.5 mm inner diameter. Demineralized water was used as the working fluid. Local gas phase parameters such as radial distribution of the void fraction, bubble frequency and bubble velocity were measured by a two-conductivity probe method located 1.61 m downstream of the beginning of the heated section. The bubble Sauter diameters (assuming spherical bubbles) were determined through the IAC, calculated using the measured bubble velocity spectrum and bubble frequency.

Numerical Details

For isothermal gas–liquid bubbly turbulent pipe flow, the generic CFD code ANSYS-CFX 11[66] was utilized to handle the two sets of equations governing conservation of mass and momentum. Numerical simulations were performed on a 60° radial sector of the pipe with symmetry boundary conditions imposed at the end vertical sides. At the test section inlet, uniformly distributed superficial liquid and gas velocities, void fraction and bubble size were specified. Details of the boundary conditions for different flow conditions are summarized in Table 1. At the pipe outlet, a relative averaged static pressure of zero was specified. A three-dimensional mesh containing hexagonal elements was generated resulting in a total of 108,000 elements over the entire pipe domain. For all flow conditions, bubble size in the range of 0–10 mm

Table 1. Bubbly Flow Conditions and Its Inlet Boundary Conditions Employed in the Present Study

Superficial liquid velocity $\langle j_f \rangle$ (m/s)	Superficial gas velocity $\langle j_g \rangle$ (m/s)		
Hibiki et al.'s[48] Experiment	Bubbly Flow Regime		Transition Regime
0.491	–	0.0556	–
$[\alpha_g\|_{z/D=0.0}(\%)]$		[10.0]	
$[D_S\|_{z/D=0.0}(\text{mm})]$		[2.5]	
0.986	0.0473	0.1130	0.242
$[\alpha_g\|_{z/D=0.0}(\%)]$	[5.0]	[10.0]	[20.0]
$[D_S\|_{z/D=0.0}(\text{mm})]$	[2.5]	[2.5]	[2.5]

was discretized into 10 bubble classes as tabulated in Table 2. The prescribed 10 size groups were further divided into two velocity fields for the *inhomogeneous* MUSIG model to predict the transition of bubbly-slug flow. Reliable convergence were achieved within 2500 iterations when the RMS (root mean square) pressure residual dropped below 1.0×10^{-7}. A fixed physical time scale of 0.002 s was adopted for all steady state simulations.

For subcooled boiling flow, numerical solutions were obtained from the two sets of transport equations governing not only mass and momentum but also energy using the generic CFD code CFX 4.4. A total number 15 bubble classes were specified for the dispersed phases in the *homogeneous* MUSIG model (see Table 2). Similar to the isothermal flow simulations, only one quarter of the annulus geometry was modeled due to the uniform prescription of the heat flux at the inner wall. A body-fitted conformal system was employed to generate the three-dimensional mesh within the annular channel resulting in a total of 13 (radial) $\times$ 30 (axial) $\times$ 3 (circumference) control volumes. A standard k–ε model was applied for both phases whereas additional turbulent viscosity induced by bubbles was included using Sato's model.[54] Because wall function was used in the present study to bridge the wall and the fully turbulent region away from heater surface, the normal distance between the wall and the first node in the bulk liquid should be such that the corresponding x^+ was greater than 30. Grid independence was examined. In the mean parameters considered, further grid refinement did not reveal significant changes to the two-phase flow parameters. Convergence was achieved within 1500 iterations when the mass residual dropped below 1.0×10^{-7}. Experimental conditions used for comparison with the simulated results are tabulated in Table 3.

Table 2. Diameter of each Discrete Bubble Class for MUSIG Model

	Central Class Diameter, d_i (mm)	
Class No.	Isothermal	Subcooled Boiling
1	0.5	0.45
2	1.5	0.94
3	2.5	1.47
4	3.5	2.02
5	4.5	2.58
6	5.5	3.14
7	6.5	3.71
8	7.5	4.27
9	8.5	4.83
10	9.5	5.40
11	–	5.96
12	–	6.53
13	–	7.10
14	–	7.66
15	–	8.23

Results and Discussion

Isothermal bubbly turbulent pipe flow results

Preliminary numerical simulations performed in this study over a range of superficial gas and liquid velocities within the bubbly flow regime have consistently resulted in the prediction of larger than expected bubble sizes. However, these results were found to clearly contradict the measurements performed by Hibiki et al.[48] as well as some experimental observations.[67,68] One plausible explanation for this discrepancy could possibly be the error embedded in the turbulent dissipation rate prediction[69] as a consequence of the turbulence model being applied contributing in turn to excessively high coalescence rates in the MUSIG model. As reported in Chen et al.,[39] similar observations also confirmed the high coalescence rates that were experienced in their bubble column study. They argued that the local coalescence rate should be reduced by an order of magnitude lower than the local breakage rate by a factor of about 10. Olmos et al.[24] further demonstrated the need to prescribe suitable calibration factor in order to aptly predict the bubble size distributions in their bubble column flow configuration. A value of 0.075 was assumed for the coalescence calibration factor. According to similar arguments stipulated above, the coalescence and breakage calibration factors (i.e. F_C and F_B), were set as 0.05 and 1.0 throughout all intended simulations of isothermal flow conditions.[27]

Local Distributions of Void Fraction and Interfacial Gas Velocity. Depending on the range of superficial velocities of gas and liquid experienced in the bubbly flow regime, the phase patterns of the vapor void fraction can be broadly categorized into four types of distributions: "wall peak", "intermediate peak", "core peak" and "transition."[70] Figure 5 compares the gas void fraction profiles obtained from the *homogeneous* MUSIG model with the experimental data measured at the location of $z/D = 53.5$ (i.e. close to the exit of channel) for three different bubbly turbulent pipe flow conditions. The high void fractions close to wall proximity typically characterized the "wall peak" behavior. Its phenomenological establishment can be best described by the balance between the positive lift force that acted to impel the bubbles away from the central core of the flow channel and the opposite effect being imposed by the lubrication force preventing the bubbles from being obliterated at the channel walls. In spite of similar trends predicted, the predicted void fraction peaks, on closer examination, appeared to be leaning more

Table 3. Subcooled Boiling Flow Conditions Measured by Yun et al.[49] Adopted in the Present Numerical Study

Case	P_{inlet} (MPa)	T_{inlet} (°C)	T_{sub} (inlet) (°C)	Q_w (kW/m^2)	G (kg/m^{2}s)
L1	0.143	96.9	13.4	152.9	474.0
L2	0.137	94.9	13.8	197.2	714.4
L3	0.143	92.1	17.9	251.5	1059.2

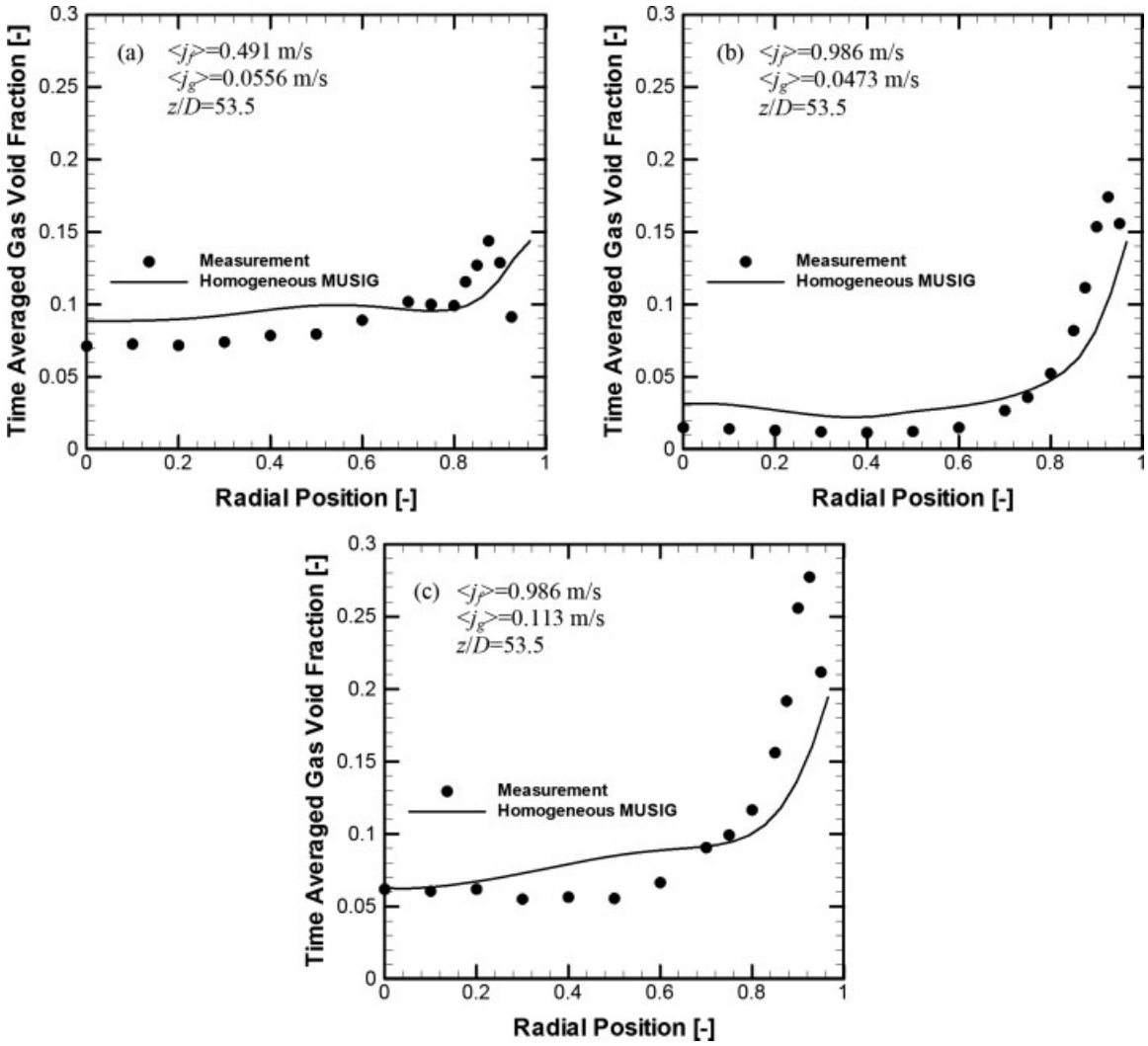

Figure 5. Predicted radial void fraction distribution and experimental data of Hibiki et al.[48] at measuring station of $z/D = 53.5$.

toward the channel wall in contrast to the actual bubble distributions observed during experiments. Against the assessment on other wall lubrication models by Frank et al.[25] and Tomiyama,[71] a much lower than expected wall force determined via Antal et al.[72] model purported to be the most probable cause of the discrepancy. As aforementioned, the two-phase turbulence modeling that could affect the magnitude of the turbulence induced dispersion force could also contribute to the additional modeling uncertainty.

Figure 6 illustrates the local interfacial gas velocity distributions at the measuring station of $z/D = 53.5$, close to the outlet of the pipe. Unlike in single phase flows, the presence of bubbles has the tendency to enhance the liquid flow turbulence intensity.[48,73] Additional turbulence being experienced at the core flattened the liquid velocity profile as expected. Through the interfacial momentum transfer, such effects are brought down to the gas phase yielding similar interfacial gas velocity profiles. In general, the interfacial gas velocity profiles for all flow conditions were found to be in good agreement with measurements, especially at the channel core. In essence, the prediction of the local bubble sizes evaluated by the coalescence and breakage kernels of the MUSIG model has a coupling effect on the phasic velocities. In better determining the Sauter mean bubble diameter, a more accurate description of the interfacial forces between the two phases should surface in more enhanced liquid/gas velocity predictions.

Local Distributions of Sauter Mean bubble Diameter, Interfacial Area Concentration and the Evolution of Bubble Size Distribution. Figure 7 illustrates the predicted and measured Sauter mean bubble diameter radial profiles at the location of $z/D = 53.5$. As measured by Hibiki et al.,[48] the Sauter mean bubble diameter profiles remained roughly unchanged throughout the whole channel. Overall, bubble size changes were found mainly due to the bubble expansion caused by the static pressure variation along the axial direction. As demonstrated by the good agreement between the predicted and the measured bubble diameters at the channel core, the ensemble bubble expansion effect was adequately captured by the two-fluid approach via the ideal gas assump-

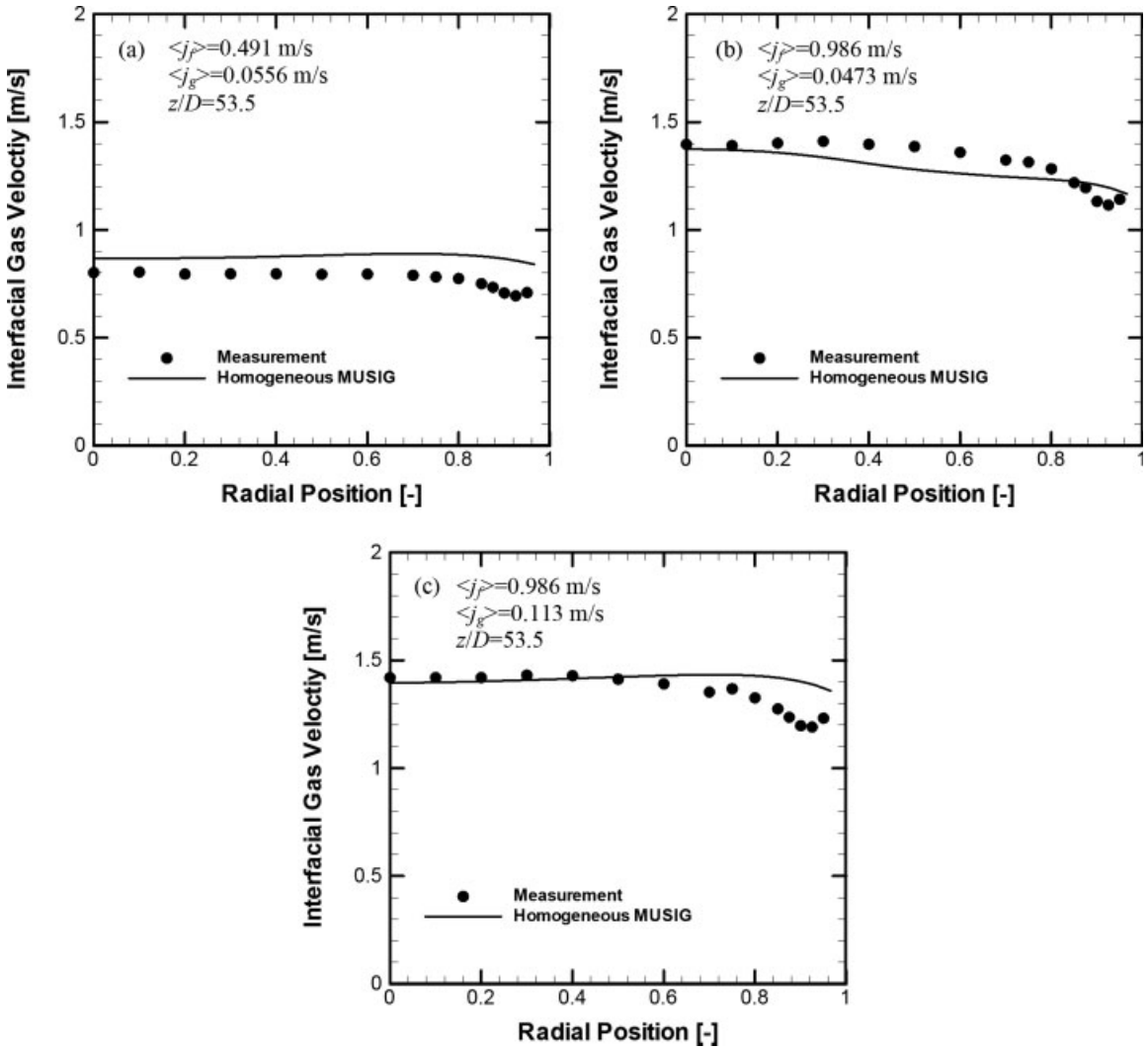

Figure 6. Predicted interfacial gas velocity distribution and experimental data of Hibiki et al.[48] at measuring station of $z/D = 53.5$.

tion. Near the wall region, slightly larger bubbles were formed due to the tendency of small bubbles migrating towards the wall thereby creating higher concentration of bubbles, increasing the likelihood of possible bubble coalescence. Remarkable agreement with the measurement at the wall region clearly illustrated the enlargement of bubble size due to bubble coalescence and bubble breakage successfully represented by the kernels in the MUSIG model. As the Sauter mean bubble diameter is closely related to the interfacial momentum forces (i.e. drag and lift forces), appropriate evaluation of the bubble diameter is thus crucial for the prediction of interfacial gas velocities.

The population balance of bubbles within the bubbly turbulent pipe flow can be further exemplified by tracking the evolution of bubble size distribution at the measuring station. Figure 8 shows the development of the size fraction of each bubble classes along the radial direction at the location of $z/D = 53.5$. Because the turbulence intensity is relatively low at the channel core (i.e. $r/R = 0.05$), bubble sizes remained unaffected owning to the insignificant bubble coalescence and bubble breakage rates. With increasing number of bubbles driven by the lift force and the rising turbulence intensity within the boundary layer towards the channel walls (i.e. $r/R = 0.8$ and 0.95), bubble coalescence and bubble breakage became increasingly noticeable forming larger bubbles and re-distributed the BSD to higher bubble classes. Such behavior was amplified especially for cases with relatively higher void fraction (e.g. Figure 8a,c).

Based on the assumption where the bubbles are spherical in shape, the local Interfacial Area Concentration (IAC) profiles may be determined based on the relation between the local void fraction and Sauter mean bubble diameter according to $a_{if} = 6\alpha_g/D_s$. The measured and predicted local interfacial area concentration profiles for the respective flow condition are shown in Figure 9. Similar to the void fraction profiles, the IAC predictions at the measuring station yielded good agreement against the measured profiles. The discrepancy between predicted results and measured data could be attributed to the error introduced by the void fraction prediction owing to the uncertainties embedded within the turbu-

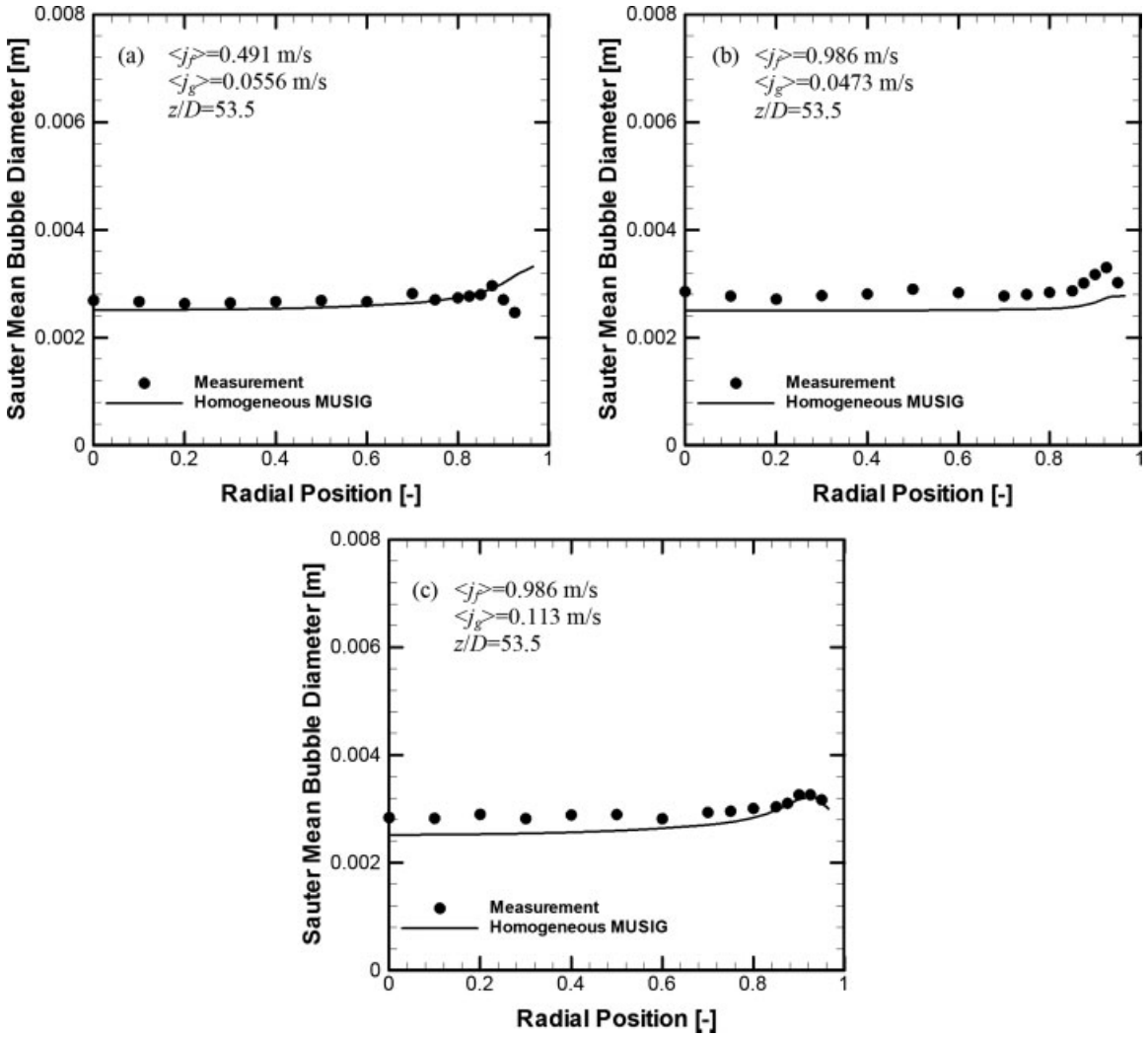

Figure 7. Predicted Sauter mean bubble diameter distribution and experimental data of Hibiki et al.[48] at measuring station of $z/D = 53.5$.

lence and wall lubrication models. Another possible cause could be the invalid assumption of spherical bubbles to aptly resolve the gas–liquid flow where large distorted bubbles prominently featured at high superficial velocities (i.e. $\langle j_f \rangle = 0.986$ m/s).

Subcooled boiling flow results

Increasing complexity of numerical simulations is now further elaborated by considering the bubble dynamics in conjunction with the heat and mass transfer processes typified by a subcooled boiling flow. For the local cases of L1, L2, and L3, the measured and predicted radial profiles of the Sauter mean bubble diameter, vapor void fraction and interfacial area concentration located at the measuring plane 1.61 m downstream of the beginning of the heated section are discussed below. In all the figures, the dimensionless parameter $(r - R_i)/(R_o - R_i) = 1$ indicates the inner surface of the unheated flow channel wall while $(r - R_i)/(R_o - R_i) = 0$ indicates the surface of the heating rod in the channel.

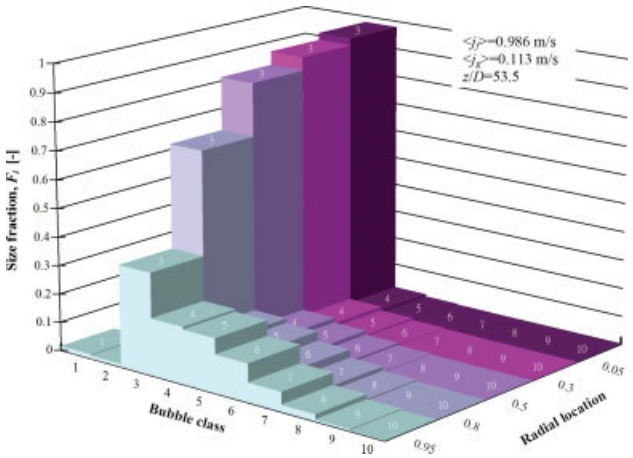

Figure 8. Predicted size fraction of each bubble classes and its evolution along radial direction at the measuring station of $z/D = 53.5$.

[Color figure can be viewed in the online issue, which is available at www.interscience.wiley.com.]

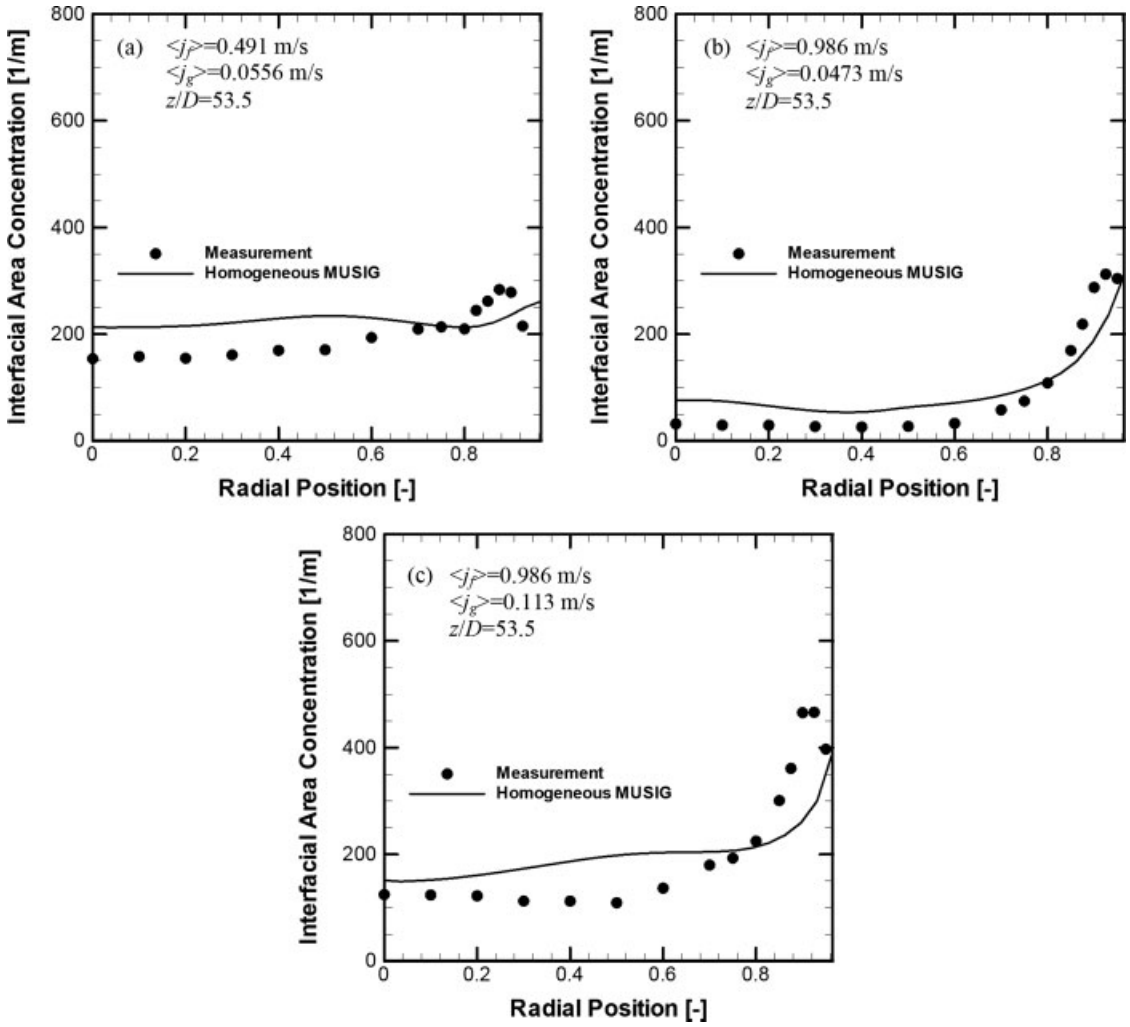

Figure 9. Predicted interfacial area concentration (IAC) distribution and experimental data of Hibiki et al.[48] at measuring station of $z/D = 53.5$.

Local Distributions of Void Fraction, Sauter Bubble Diameter and Interfacial Area Concentration. Figure 10 illustrates the predicted Sauter mean bubble diameter profiles at the measuring plane of the heated annular channel. Experimental data and observations[50,74] suggested that vapor bubbles, relatively small when detached from the heated surface, have the tendency of significantly colliding with other detached bubbles at the downstream and subsequently forming bigger bubbles via coalescence. For all three cases, the bubble size changes were found to be adequately predicted by the modified MUSIG model. Observed consistent trends between the predicted and measured Sauter mean bubble diameter reflected the measure of the modified MUSIG model in aptly capturing the bubble coalescence especially in the vicinity of the heated wall. The development of bubbles in this region stemmed from the evaporation process occurring at the heated wall and forces acting on the vapor bubbles determining the bubble size at departure or lift-off. Table 4 illustrates the various contributing heat flux components and the associated bubble departure and lift-off diameters evaluated by the improved heat partition model. On the basis of the force balance model, the bubble departure diameter was predicted with a size of ~0.56–0.58 mm whereas the lift-off diameters were found to range from 1.2 to 1.45 mm. The ratio between the bubble lift-off diameter and bubble departure diameter was thus ascertained to be between 2 and 3, which incidentally closely corresponded to experimental observations of Basu et al.[60] Surface quenching due to sliding bubbles and evaporation were found to be the dominant modes of heat transfer governing the heat partition model. The former highlighted the prevalence of bubble sliding motions on the surface significantly altering the rate of heat transfer and subsequently the resultant vapor generation rate. Away from the heated wall, bubbles entering the bulk subcooled liquid were condensed due to the subcooling effect. Predicted trends of the Sauter mean diameter profiles clearly showed the gradual collapse of the bubbles from the channel centre to the outer unheated wall. The over-prediction of the bubble diameters for cases L1 and L2 could be attributed by the underestimation of the subcooling condensation, which was determined by an empirical correlation based on the Nusselt number description.

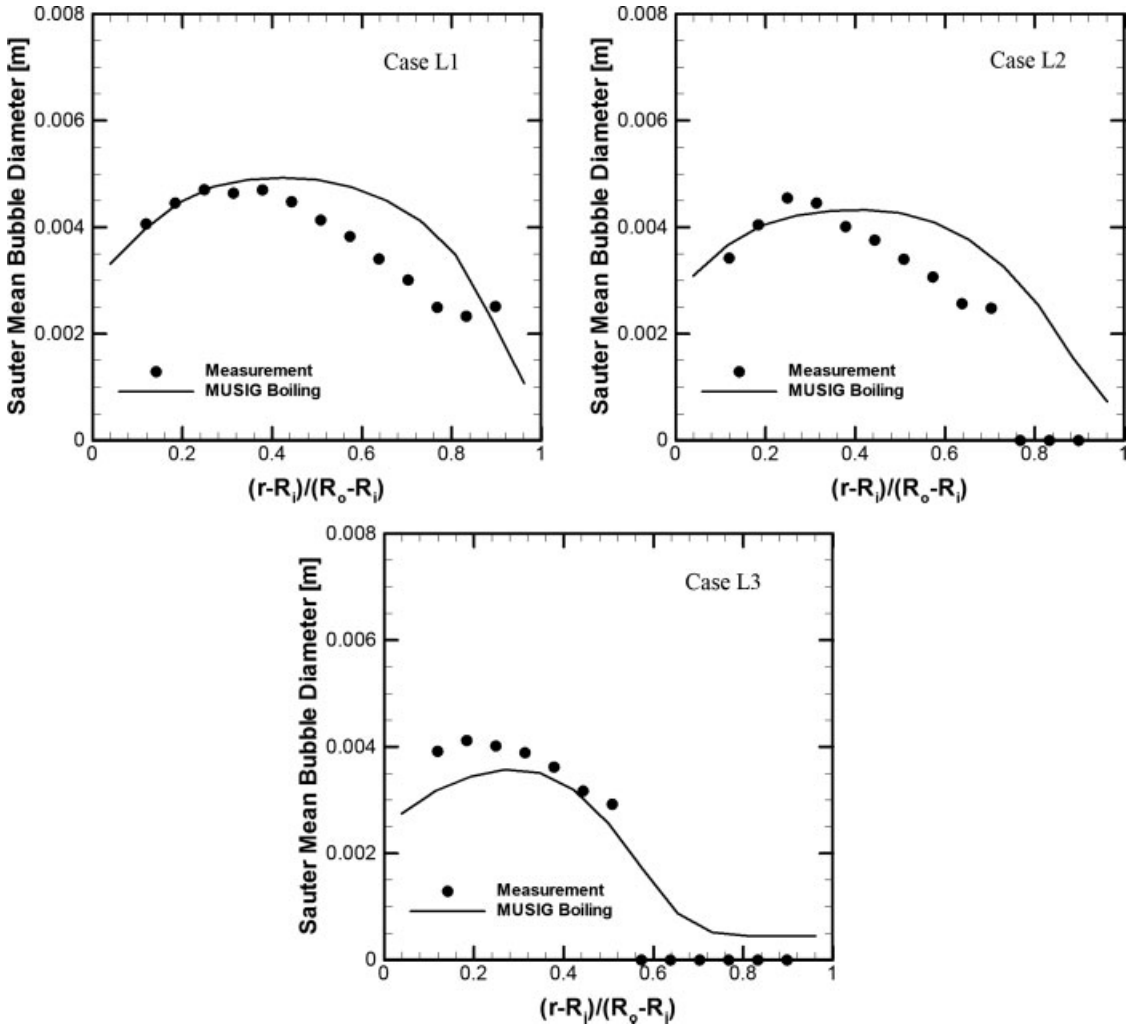

Figure 10. Prediction Sauter mean bubble diameter distribution and experimental data at the measuring station.

Although the measured bubble sizes near the heated wall were found to agree rather well with the measured data confirming to certain extend the appropriate estimation of the bubble lift-off diameters, a closer examination of the local void fraction profiles at the measuring station in Figure 11 indicated a less than satisfactory prediction of the void fraction near the heated surface where they were either over- or under-predicted as exemplified in cases L1 and L3. The void fraction distribution in case L2 compared nonetheless reasonably well with measurement. This discrepancy could be attributed to the uncertainties within the heat partition model in specifically evaluating the vapor generation rate. In the quest of reducing the application of empirical correlations, the consideration of the active nucleation site density in the present study still depended on the use of an appropriate relationship, which could be sensitive to the flow conditions. The significance of active wall nucleation site density linking to the prediction of the IAC has also been reported in Hibiki and Ishii.[75] Nevertheless, as the population of cavities may vary significantly between materials and cannot be measured directly, an adequate expression of the active nucleation site density covering a wide range of flow conditions remains outstanding and more concerted research is required. The IAC profiles as shown in Figure 12 also exhibited similar trends with the void fraction distributions plotted in Figure 11.

Evolution of Bubble Size Distribution and Bubble Generation Rate due to Coalescence, Breakage, and Condensation. Figure 13 shows the bubble size distribution expressed in terms of interfacial area concentration of individual bubbles classes along radial direction for the case L3 at the measuring station describes the bubble dynamics caused by coalescence, breakage and condensation in subcooled boiling

Table 4. Predicted Heat Partitions, Bubble Departure and Lift-Off Diameter of Subcooled Boiling Flow Conditions

	Case		
	L1	L2	L3
Measuring location			
Q_c (W/m^2) (%)	0	0	0
Q_{tc} (W/m^2) (%)	2.51	4.56	6.42
Q_{tcsl} (W/m^2) (%)	55.07	61.25	65.58
Q_e (W/m^2) (%)	42.42	34.19	28.00
D_d (mm)	0.56	0.58	0.57
D_l (mm)	1.45	1.31	1.20

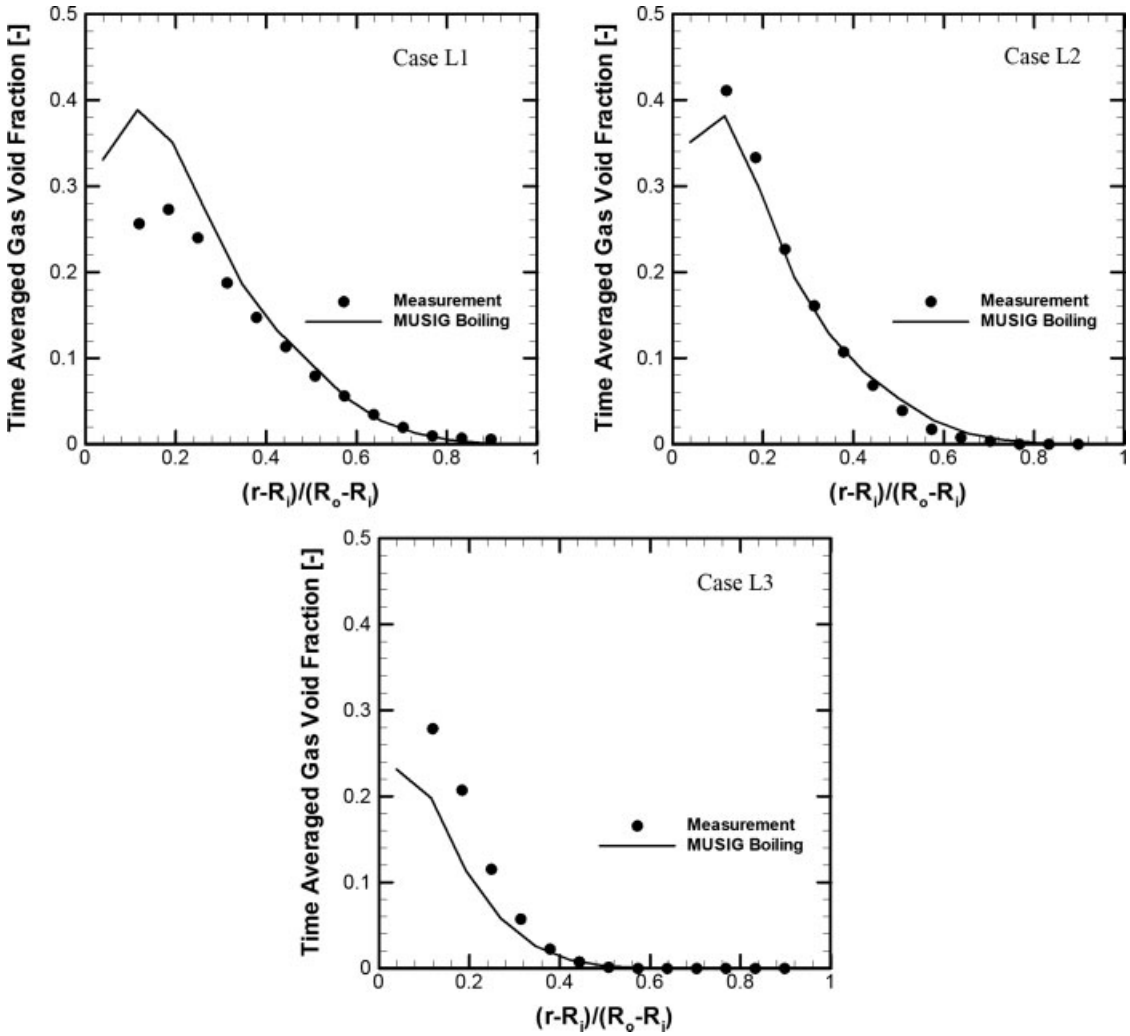

Figure 11. Predicted radial void fraction distribution and experimental data at the measuring station.

flows. Significant vapor bubbles represented from bubble class 3 in the vicinity of the heated wall essentially indicated the size of the bubble lift-off diameter which coalesced with downstream/neighboring bubbles forming larger void fraction peaks as indicated by bubble classes of 7 and 9. Owing to the high shear stress within the boundary layer, some bubbles are affected by turbulent impact due to breakage resulting in the formation of smaller bubbles as evidenced by the significant distributions indicated within bubble classes 1 and 2. Away from the heated wall, the condensation process dominated in reducing the void fraction of each bubble classes and eventually collapsing majority of the bubbles beyond the position $(r - R_i)/(R_o - R_i) = 0.6$. The net generation rate due to coalescence and breakage and condensation rate of selected bubble classes are depicted in Figure 14. Close to the wall region, the highest generation rate corresponding to the peak value observed in Figure 13 is represented by bubble class 7; substantial generation rate was also found for bubble class 3 at the same region. Although the coalescence of bubbles was seen to be governed mainly by bubble classes 3 and 7, bubble classes 3 and 12 also contributed to the condensation process due to their considerably high number density and interfacial area. These two figures aptly demonstrated the mechanisms of coalescence, breakage and condensation in the modified MUSIG model affecting the thermo-mechanical and hydrodynamics processes within the subcooled boiling flow.

Limitations and shortcomings of existing models

Encouraging predictions by the homogeneous MUSIG and modified MUSIG models clearly demonstrated their viable applications in resolving isothermal bubbly turbulent pipe flow and subcooled boiling conditions. Nevertheless, the flow cases that have been investigated from above generally possessed only weak bubble–bubble interactions and narrow bubble size distributions. Specifically, the limitation involved solving a single velocity field for all bubble classes. To circumvent the problem, the inhomogeneous MUSIG model,[29] which divides the gaseous dispersed phase into N number of velocity groups, was further assessed to evaluate its feasibility in handling bubbly-to-slug transition flow regime.

Transitional flow condition with liquid superficial velocity $\langle j_f \rangle = 0.986$ m/s and gas superficial velocity $\langle j_g \rangle = 0.242$ m/s as measured by Hibiki et al.[48] was investigated for

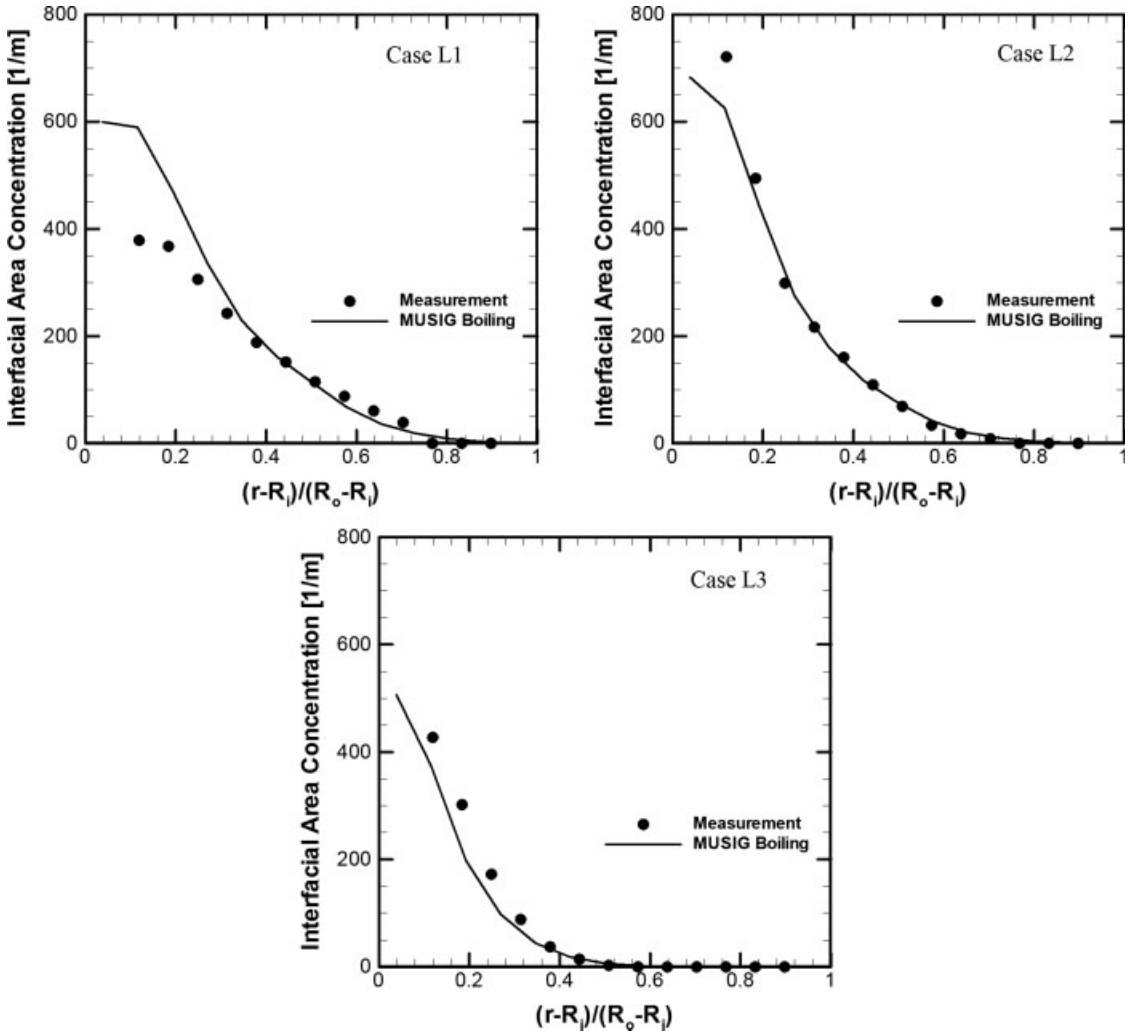

Figure 12. Predicted interfacial gas velocity distribution and experimental data at the measuring station.

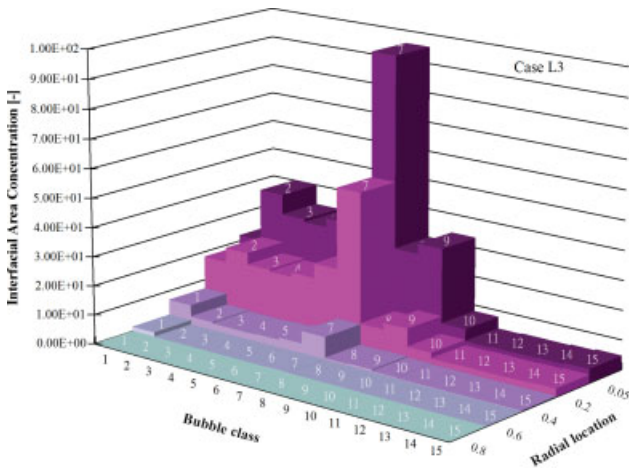

Figure 13. Predicted IAC of each bubbles class along radial direction for the case L3 at the measuring station.

[Color figure can be viewed in the online issue, which is available at www.interscience.wiley.com.]

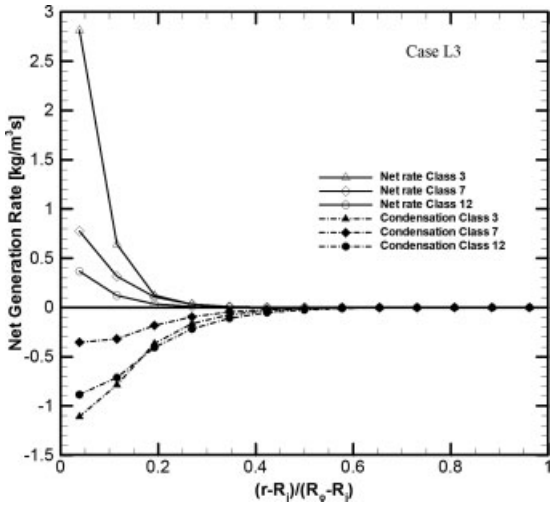

Figure 14. Predicted net bubble generation rate due to coalescence and breakage and condensation rate of selected bubble classes of modified MUSIG model.

the application of both the *homogeneous* and *inhomogeneous* MUSIG models. Similar to the bubbly turbulent pipe flow simulations presented in previous section, the same boundary conditions were specified for both models where details can be referred in Table 1. Bubble size in the range of 0–10 mm discretized into 10 sub-size groups as tabulated in Table 2 was similarly considered. For the inhomogeneous model, two velocity fields were solved representing the traveling speed of small and big bubbles. The first five bubble classes (range of 0–5 mm) were assigned to the first velocity field while the remaining bubble classes (range of 5–10 mm) were assigned to the second velocity field. Sensitivity studies on the increasing resolution greater than two velocity fields were also performed. With regards to the mean parameters investigated, negligible differences were nonetheless found.

The measured and predicted local radical void fraction, Sauter mean bubble diameter, IAC and gas velocity distribution at the measuring station of $z/D = 53.5$ are illustrated in Figure 15. Comparing the predicted Sauter mean diameters, the inhomogeneous MUSIG model was found to yield comparatively better prediction when compared against the measured data. This could be attributed to the merit of splitting the bubble velocity with two independent fields which facilitated the model to re-capture the separation of small and big bubbles caused by different lift force actuation. Nevertheless, notable discrepancies were found when comparing against other variables (i.e. void fraction, gas velocity and IAC) against the experimental measurements. As depicted in Figure 15b, void fractions of both models were obviously over-predicted at the channel core but under-predicted at the wall region, which resulted in unsatisfactory IAC predictions (see Figure 15c). Interestingly enough, the consideration of multiple velocity fields in the inhomogeneous MUSIG model did not contribute to the desired expected improvements when comparing the gas velocity predictions against those of the homogeneous MUSIG model (see Figure 15d). This could be possibly due to the interfacial force models which have been developed principally for isolated bubbles rather than on a swarm or cluster of bubbles. Direct applications of these models for high void fraction conditions, where bubbles are closely packed, become questionable and introduce uncertainties in the model calculations. Such findings have also been reported lately in the experimental work by Simonnet et al.[76] Based on their measurements, they concluded that the

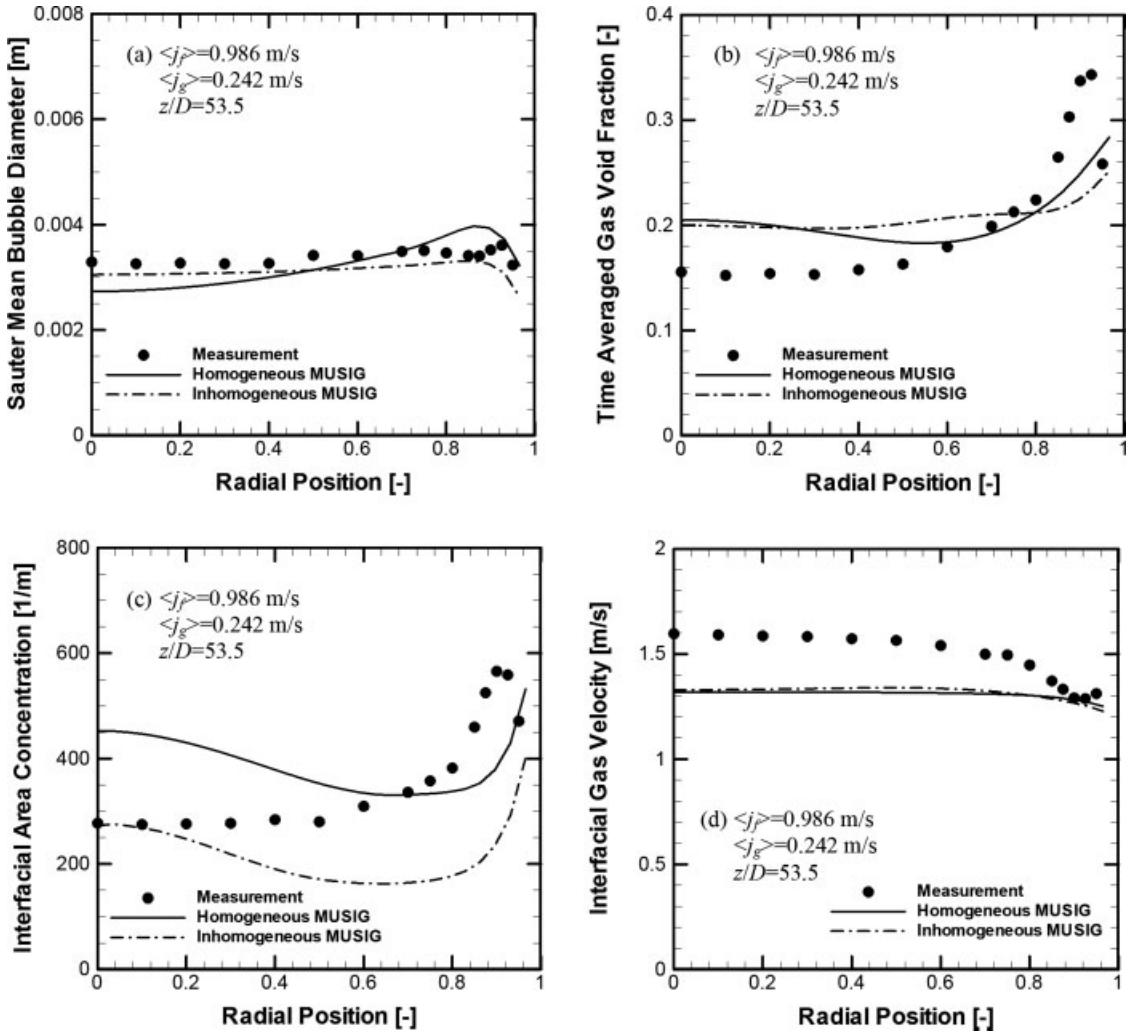

Figure 15. Predicted local radical void fraction, Sauter mean bubble diameter, IAC and gas velocity distribution of transition bubbly-to-slug flow condition by *homogenous* and *inhomogeneous* MUSIG model.

aspiration of bubbles in the wake of the leading ones became dominant if the void fraction exceeded the critical value 15%. This caused a sharp increase of the relative velocity of bubbles and significantly altered the associated drag coefficient. Interfacial forces models based on empirical correlations of isolated spherical bubbles have also been found to be not appropriate[77,78] for high void fraction conditions, As high void fraction (i.e. 20%) condition has been simulated here, the ambiguity of the interfacial drag forces could plausibly be the main source of error. Furthermore, the wall lubrication force could be under-predicted by the Antal's model[79] which could represent another source of error in calculating lateral interfacial forces.[80]

On the other hand, coalescence due to wake entrainment and breakage of large bubbles caused by surface instability may prevail beyond the critical void fraction limit. The existing kernels which only featured coalescence due to random collision and breakage due to turbulent impact for spherical bubbles have to be extended to account for additional bubble mechanistic behaviors for cap/slug bubbles. Several papers in the literature have attempted to deal with this problem by the development of a two-group interfacial area transport equation.[81–84] Encouraging results attained thus far not only suggested the feasibility of the proposed approach but more importantly the prevalence of large bubble mechanisms that are substantially different from spherical bubble interactions in turbulent gas–liquid flows.

Conclusions

With the mounting interest of solving PBE for gas–liquid flows, a complete three-dimensional two-fluid model coupled with the class method of population balance approach was presented to handle the complex hydrodynamics and thermo-mechanical processes of various bubbly turbulent pipe flow conditions. Numerical study of isothermal bubbly turbulent pipe flows in a vertical pipe was first studied in order to confine the complexity of solely modeling the bubble coalescence and bubble breakage mechanisms. The homogenous MUSIG model which assumed all bubbles traveling with the same velocity was applied. Comparison of the predicted results was made against the measurements of Hibiki et al.[48] Overall, the homogeneous MUSIG model yielded good agreement for the local radial distributions of void fraction, interfacial area concentration, Sauter mean bubble diameter and gas and liquid velocities against measurements. Numerical results also clearly showed that the range of bubbles sizes existed in the gas–liquid flows required substantial resolution. Numerical results obtained through this study clearly demonstrated the competence of the MUSIG model and the robustness of the bubble coalescence and bubble breakage kernels in accommodating the interactions of finely dispersed bubbles within isothermal bubbly turbulent pipe flows.

The potential of the population balance approach was further exploited in modeling subcooled boiling flows. Such flows by nature are inherently complex since they simultaneously embrace all complex flow hydrodynamics, bubble coalescence and bubble breakage accompanied by heat and mass transfer processes in the bulk flow, and various surface heat flux characterizations. An improved heat partition model which mechanistically determined the bubble departure and lift-off diameter was also presented as a closure for the problem in order to determine the appropriate evaporation rate of the nucleation process. Numerical results validated against the experiment data of Yun et al.[49] and Lee et al.[50] for low-pressure subcooled boiling annular channel flows showed good agreement for the local Sauter mean bubble diameter, void fraction, IAC profiles. Detailed vapor size distribution and its corresponding generation rates were probed via the size fractions of the modified MUSIG model in order to better envisage the condensation effect in conjunction with the occurrence of bubble coalescence and bubble breakage within the gas–liquid flow.

In addition to the homogeneous MUSIG model, inhomogeneous MUSIG model was also applied to investigate the feasibility of application in handling transition bubbly-to-slug flow. It was observed that the inhomogeneous MUSIG gave better prediction of the Sauter mean bubble diameter distributions when compared to the homogeneous model. The more complicated inhomogeneous MUSIG model provided the premise of better capturing the different effects of the lift force acting on the small and large bubbles. Less encouraging results were however ascertained between the predicted and measured void fraction, interfacial gas velocity and IAC profiles. One plausible explanation could be the departure from the ideal finely dispersed spherical bubble assumption to more realistic flows of highly close packed distorted bubbles. Existing interfacial forces models, which have been calibrated from isolated spherical bubbles, may not be strictly applicable for such flows especially when the peak void fraction exceeds 15%. Recent experimental study correlating the drag coefficients with the void fraction demonstrated the importance of such development.[76]

Although encouraging results had been obtained from the MUSIG model based on CM, QMOM or other moment methods which represent a rather sound mathematical approach and an elegant tool of solving the PBE with limited computational burden could be alternatively considered for modeling practical bubbly flows for future investigative studies.

Acknowledgment

The financial support provided by the Australian Research Council (ARC project ID DP0556094) is gratefully acknowledged.

Notation

a_{if} = interfacial area concentration
A_c = cross-sectional area of the boiling channel
A_q = fraction of heater area occupied by bubbles
C_1, C_2 = constants defined in Eq. 35
C_D = drag coefficient
C_L = shear lift coefficient
C_p = specific heat
C_s = constant defined in Eq. 44
C_v = Acceleration coefficient
d = vapor bubble diameter at heated surface
d_w = surface/bubble contact diameter
D = average bubble diameter
D_c,D_B = bubble death rate due to coalescence and breakage
D_b = departing bubble diameter
D_d = bubble departure diameter
D_l = bubble lift-off diameter
D_s = Sauter mean bubble diameter
f = bubble generation frequency

f_i = scalar size fraction of the ith discrete bubble classes $f_i = \alpha_i / \alpha_g$
F = degree of surface cavity flooding
F_c,F_B = calibration factors for coalescence and breakage
F_b = buoyancy force
F_{cp} = contact pressure force
F_{du} = unsteady drag force due to asymmetrical growth of the bubble
F_h = force due to the hydrodynamic pressure
F_{qs} = Quasi-steady-drag force
F_s = surface tension force
F_{sL} = shear lift force
F_{lg} = action of interfacial forces from vapor on liquid
F_{gl} = action of interfacial forces from liquid on vapor
F_{lg}^{drag} = drag force
F_{lg}^{lift} = lift force
$F_{lg}^{lubrication}$ = wall lubrication force
$F_{lg}^{dispersion}$ = turbulent dispersion force
g = gravitational constant
$\vec{g}$ = gravitational vector
G = mass flux
G_s = dimensionless shear rate
h = interfacial heat transfer coefficient
h_0, h_f = initial and critical film thickness
h_{fg} = latent heat
H = enthalpy
Ja = Jakob number
k = thermal or turbulent kinetic energy
K = projected area of bubble
h_{fg} = latent heat of vaporization
l_s = sliding distance
n_i = number density of the discrete bubble ith class
N_a = active nucleation site density
P = pressure
P_k = turbulent kinetic energy production term
P_c,P_B = bubble production rate due to coalescence and breakage
Q_w = wall heat flux
Q_c = heat transfer due to forced convection
Q_e = heat transfer due to evaporation
Q_{tc} = heat transfer (transient conduction) due to stationary bubble
Q_{tcsl} = heat transfer (transient conduction) due to sliding bubble
r = bubble radius at heated wall or flow spacing within annular channel
r_c = cavity radius at heated surface
r_r = curvature radius of the bubble at heated surface
R = source/sink term due to coalescence and breakage
Re = bubble Reynolds number
R_f = ratio of the actual number of bubbles lifting off to the number of active nucleation sites
R_{ph} = source/sink term due to phase change
R_i = radius of inner heated wall
R_o = radius of outer unheated wall
s = spacing between nucleation sites
S_i = additional source terms due to coalescence and breakage
S_{ij} = tensor of shear stress
St = Stanton number
t = time
t_g = bubble growth period
t_{sl} = bubble sliding period
t_w = bubble waiting period
T = temperature
ΔT = difference in temperature
u = velocity
$\vec{u}$ = velocity vector
u_τ = friction velocity
v_i = specific volume of discrete bubble i^{th} class
x = Cartesian coordinate along x
x^+ = non-dimensional normal distance from heated wall
y = Cartesian coordinate along y

Greek letters

α = advancing angle
α_g = vapor void fraction
α_l = liquid void fraction
β = receding angle
χ = coalescence rate
δ_l = Thermal boundary layer thickness
ε = turbulent dissipation rate
ϕ_{WN} = bubble nucleation rate
ϕ_{COND} = bubble condensation rate
η = thermal diffusivity or coalescence volume matrix defined in Eq. (19)
λ = size of an eddy
λ^e = effective viscosity
μ = viscosity
θ = bubble contact angle
θ_i = inclination angle
ρ = density
σ = surface tension/Prandtl number
τ_{ij} = bubble contact time
ω = turbulent frequency
Ω = breakage rate
ξ = size ratio between an eddy and a particle in the inertial subrange
ξ_H = heated perimeter of boiling channel
Γ_{lg} = interfacial mass transfer from vapor to liquid
Γ_{gl} = interfacial mass transfer from liquid to vapor

Subscripts

axial = axial distribution
g = vapor
inlet = channel entrance
l = liquid
local = local distribution
s = surface heater
t = turbulent
sat = saturation
sub = subcooled
sup = superheated
w = heated surface wall

Literature Cited

1. Liu TJ, Bankoff SG. Structure of air-water bubbly flow in a vertical pipe - I. Liquid mean velocity and turbulence measurements. *Int J Heat Mass Transfer*. 1993;36:1049–1060.
2. Zeitoun O, Shoukri M. Bubble behavior and mean diameter in subcooled flow boiling. *ASME J Heat Transfer*. 1996;118:110–116.
3. Kashinsky ON, Randin VV. Downward bubbly gas–liquid flow in a vertical pipe. *Int J Multiphase Flow*. 1999;25:109–138.
4. Matos A, de Rosa ES, Franca FA. The phase distribution of upward co-current bubbly flows in a vertical square channel. *J Braz Soc Mech Sci Eng*. 2004;26:308–316.
5. Biswas S, Esmaeeli A, Tryggvason G. Comparison of results from DNS of bubbly flows with a two-fluid model for two dimensional laminar flows. *Int J Multiphase Flow*. 2005;31:1036–1048.
6. Lu J, Biswas S, Tryggvason G. A DNS study of laminar bubbly flows in a vertical channel. *Int J Multiphase Flow*. 2006;32:643–660.
7. Bove S, Solberg T, Hjertager BH. A novel algorithm for solving population balance equations: the parallel parent and daughter classes. Derivation, analysis and testing. *Chem Eng Sci*. 2005;60:1449–1464.
8. Hulburt HM, Katz S. Some problems in particle technology: a statistical mechanical formulation. *Chem Eng Sci*. 1964;19:55–574.
9. Frenklack M, Harris SJ. Aerosol dynamics modelling using the method of moments. *J Colloid Interface Sci*. 1987;118:252–261.
10. Frenklack M. Method of moments with interpolative closure. *Chem Eng Sci*. 2002;57:2229–2239.
11. McGraw R. Description of aerosol dynamics by the quadrature method of moments. *Aerosol Sci Technol*. 1997;27:255–265.
12. Gordon RG. Error bounds in equilibrium statistical mechanics. *J Math Phys*. 1968;9:655–672.
13. McGraw E, Wright DL. Chemically resolved aerosol dynamics for internal mixtures by the quadrature method of moments. *J Aerosol Sci*. 2003;34:189–209.

14. Marchisio DL, Fox RO. Solution of population balance equations using the direct quadrature method of moments. *J Aerosol Sci*. 2005;36:43–73.
15. Grosch R, Briesen H, Marquardt W, Wulkow M. Generalization and numerical investigation of QMOM. *AIChE J*. 2007;53:207–227.
16. Barrett JC, Webb NA. A comparison of some approximate methods for solving the aerosol general dynamics equation. *J Aerosol Sci*. 1998;29:31–39.
17. Marchisio DL, Vigil DR, Fox RO. Quadrature method of moments for aggregation-breakage processes. *J Colloid Interface Sci*. 2003; 258:322–324.
18. Marchisio DL, Pikturna JT, Fox RO, Vigil RD. Quadrature method for moments for population-balance equations. *AIChE J*. 2003;49: 1266–1276.
19. Marchisio DL, Vigil DR, Fox RO. Implementation of the quadrature method of moments in CFD codes for aggregation-breakage problems. *Chem Eng Sci*. 2003;58:3337–3351.
20. Marchisio DL, Fox RO. Solution of population balance equations using the direct quadrature method of moments. *J Aerosol Sci*. 2005;36:43–73.
21. Ervin EA, Tryggvason G. The rise of bubbles in a vertical shear flow. *J Fluids Eng*. 1997;119:443–449.
22. Bothe D, Schmidtke M, Warnecke HJ. VOF-Simulation of the life force for single bubbles in simple shear flow. *Chem Eng Technol*. 2006;29:1048–1053.
23. Pochorecki R, Moniuk W, Bielski P, Zdrojkwoski A. Modelling of the coalescence/redisperison processes in bubble columns. *Chem Eng Sci*. 2001;56:6157–6164.
24. Olmos E, Gentric C, Vial Ch, Wild G, Midoux N. Numerical simulation of multiphase flow in bubble column. Influence of bubble coalescence and break-up. *Chem Eng Sci*. 2001;56:6359–6365.
25. Frank T, Shi J, Burns AD. Validation of eulerian multiphase flow models for nuclear safety application. In *Proceeding of the Third International Symposium on Two-Phase Modelling and Experimentation*, Pisa, Italy, 2004.
26. Yeoh GH, Tu JY. Thermal-hydrodynamic modelling of bubbly flows with heat and mass transfer. *AIChE J*. 2005;51:8–27.
27. Cheung SCP, Yeoh GH, Tu JY. On the numerical study of isothermal vertical bubbly flow using two population balance approaches. *Chem Eng Sci*. 2007;62:4659–4674.
28. Sanyal J, Marchisio DL, Fox RO, Dhanasekharan K. On the comparison between population balance models for CFD simulation of bubble column. *Ind Eng Chem Res*. 2005;44:5063–5072.
29. Krepper E, Lucas D, Prasser H. On the modelling of bubbly flow in vertical pipes. *Nucl Eng Des*. 2005;235:597–611.
30. Prince MJ, Blanch HW. Bubble coalescence and break-up in air sparged bubble columns. *AIChE J*. 1990;36:1485–1499.
31. Chesters AK, Hoffman G. Bubble coalescence in pure liquids. *Appl Sci Res*. 1982;38:353–361.
32. Luo H, Svendsen H. Theoretical model for drop and bubble breakup in turbulent dispersions. *AIChE J*. 1996;42:1225–1233.
33. Lehr F, Mewes D. A transport equation for the interfacial area density applied to bubble column. *Chem Eng Sci*. 2001;56:1159–1166.
34. Hagesaether L, Jakobsen H, Svendsen HF. A model for turbulent binary breakup of dispersed fluid particles. *Chem Eng Sci*. 2002;57: 3251–3267.
35. Wang T, Wang J, Jin Y. A novel theoretical breakup kernel function for bubbles/droplets in a turbulent flow. *Chem Eng Sci*. 2003;58: 4629–4637.
36. Wang T, Wang J, Jin Y. Theoretical prediction of flow regime transition in bubble columns by the population balance model. *Chem Eng Sci*. 2005;60:6199–6209.
37. Wang T, Wang J, Jin Y. A CFD-PBM coupled model for gas–liquid flows. *AIChE J*. 2006;52:125–140.
38. Andersson R, Andersson B. Modeling the breakup of fluid particles in turbulent flows. *AIChE J*. 2006;52:2031–2038.
39. Chen P, Sanyal J, Dudukovíc MP. Numerical simulation of bubble columns flows: effect of different breakup and coalescence closures. *Chem Eng Sci*. 2005;60:1085–1101.
40. Yeoh GH, Tu JY. Population balance modelling for bubbly flows with heat and mass transfer. *Chem Eng Sci*. 2004;59:3125–3139.
41. Sha Z, Laari A, Turunen I. Multi-phase-multi-group model for the inclusion of population balances in to CFD simulation of gas–liquid bubble flows. *Chem Eng Technol*. 2006;29:550–559.
42. Bordel S, Mato R, Villaverade S. Modeling of the evolution with length of bubble size distributions in bubble columns. *Chem Eng Sci*. 2006;61:2663–2673.
43. Jia X, Wen J, Zhou H, Fend W, Yuan Q. Local hydrodynamics modelling of a gas–liquid–solid three phase bubble column. *AIChE J*. 2007;53:2221–2231.
44. Klausner JF, Mei R, Bernhard DM, Zeng LZ. Vapor bubble departure in forced convection boiling. *Int J Heat Mass Transfer*. 1993;36:651–662.
45. Gopinath R, Basu N, Dhir VK. Interfacial heat transfer during subcooled flow boiling. *Int J Heat Mass Transfer*. 2002;45:3947–3959.
46. Anglart H, Nylund O. CFD application to prediction of void distribution in two-phase bubbly flows in rod bundles. *Nucl Sci Eng*. 1996;163:81–98.
47. Yeoh GH, Tu JY. Numerical modelling of bubbly flows with and without heat and mass transfer. *Appl Math Modell*. 2006;30:1067–1095.
48. Hibiki T, Ishii M, Xiao Z. Axial interfacial area transport of vertical bubble flows. *Int J Heat Mass Transfer*. 2001;44:1869–1888.
49. Yun BJ, Park G-C, Song CH, Chung MK. Measurements of local two-phase flow parameters in a boiling flow channel. In *Proceedings of the OECD/CSNI Specialist Meeting on Advanced Instrumentation and Measurement Techniques*. 1997.
50. Lee TH, Park G-C, Lee DJ. Local flow characteristics of subcooled boiling flow of water in a vertical annulus. *Int J Multiphase Flow*. 2002;28:1351–1368.
51. Yeoh GH, Cheung SCP, Tu JY, Ho MKM. Fundamental consideration of wall heat partition of vertical subcooled boiling flows. *Int J Heat Mass Transfer*. 2008; In press.
52. Tu JY, Yeoh GH. On numerical modelling of low-pressure subcooled boiling flows. *Int J Heat Mass Transfer*. 2002;45:1197–1209.
53. Menter FR. Two-equation eddy viscosity turbulence models for engineering applications. *AIAA J*. 1994;32:1598–1605.
54. Sato Y, Sadatomi M, Sekoguchi K. Momentum and heat transfer in two-phase bubbly flow - I. *Int J Multiphase Flow*. 1981;7:167–178.
55. Lo S. Application of the MUSIG model to bubbly flows. *AEAT-1096*, AEA Technology, June 1996.
56. Shi JM, Zwart PJ, Frank T, Rohde U, Prasser HM. Development of a multiple velocity multiple size group model for poly-dispersed multiphase flows. In *Annual Report of Institute of Safety Research*. Forschungszentrum Rossendorf, Germany, 2004.
57. Krepper E, Frank T, Lucas D, Prasser H, Zwart PJ. Inhomogeneous MUSIG model - a Population Balance approach for polydispersed bubbly flows. In, *Proceeding of the 6th International Conference on Multiphase Flow*. Leipzig, Germany, 2007.
58. Rotta JC. *Turbulente Stromungen*. Teubner, BG: Stuttgart, 1972.
59. Judd RL, Hwang KS. A comprehensive model for nucleate pool boiling heat transfer including microlayer evaporation. *ASME J Heat Transfer*. 1976;98:623–629.
60. Basu N, Warrier GR, Dhir VK. Wall heat flux partitioning during subcooled flow boiling, Part I: Model development. *ASME J Heat Transfer*. 2005;127:131–140.
61. Konîcar B, Kljenak I, Mavko B. Modeling of local two-phase parameters in upward subcooled flow boiling at low pressure. *Int J Heat Mass Transfer*. 2004;47:1499–1513.
62. Hsu YY, Graham RW. *Transport Process in Boiling and Two-phase Systems*. Hemisphere: Washington, 1976.
63. Zeng LZ, Klausner JF, Bernhard DM, Mei R. A unified model for the prediction of bubble detachment diameters in boiling systems - II. Flow boiling. *Int J Heat Mass Transfer*. 1993;36:2271–2279.
64. Zuber N. The dynamics of vapor bubbles in nonuniform temperature fields. *Int J Heat Mass Transfer*. 1961;2:83–98.
65. Steiner H, Kobor A, Gebhard L. A wall heat transfer model for subcooled boiling flow. *Int J Heat Mass Transfer*. 2005;48:4161–4173.
66. ANSYS. *CFX-11 User Manual*. ANSYS-CFX. 2006.
67. Bukur DB, Daly JG, Patel SA. Application of γ-ray attenuation for measurement of gas hold-ups and flow regime transitions in bubble columns. *Ind Eng Chem Res*. 1996;35:70–80.
68. George DL, Shollenberger KA, Torczynski, JR. Sparger effect on gas volume fraction distributions in vertical bubble-column flows as measured by gamma-densitometry tomography. In *ASME 2000 Fluid Engineering Division Summer Meeting*. Boston: USA, 2000.
69. Bertola F, Grundseth J, Hagesaether L, Dorao C, Luo H, Hjarbo KW, Svendsen HF, Vanni MB, Jakobsen HA. Numerical analysis

and experimental validation of bubble size distributions in two phase bubble column reactors. In *Proceedings of the Third European-Japanese Two Phase Flow Group Meeting*. Certosa di Pontignano, 2003.
70. Serizawa A, Kataoka I. Phase distribution in two-phase flow. In: Afgan NH, editor. *Transient Phenomena in Multiphase Flow*. Washington DC, 1988.
71. Tomiyama A. Struggle with computational bubble dynamics. In *Proceeding of the Third International Conference on Multiphase Flow*. Lyon: France, 1998.
72. Antal SP, Lahey RT Jr, Flaherty JE. Analysis of phase distribution in fully developed laminar bubbly two-phase flow. *Int J Multiphase Flow*. 1991;17:635–652.
73. Serizawa A, Kataoka I. Turbulence suppression in bubbly two-phase flow. *Nucl Eng Des*. 1990;122:1–16.
74. Bonjour J, Lallemand M. Two-phase flow structure near a heated vertical wall during nucleate pool boiling. *Int J Multiphase Flow*. 2001;28:1–19.
75. Hibiki T, Ishii M. Active nucleation site density in boiling systems. *Int J Heat Mass Transfer*. 2003;46:2587–2601.
76. Simonnet M, Gentric C, Olmos E, Midoux N. Experimental determination of the drag coefficient in a swarm of bubbles. *Chem Eng Sci*. 2007;62:858–866.
77. Jakobsen H. Phase distribution phenomena in two-phase bubble column reactors. *Chem Eng Sci*. 2001;56:1049–1056.
78. Behzadi A, Issa R, Rusche H. Modelling of dispersed bubble and droplet flow at high phase fractions. *Chem Eng Sci*. 2004;59:759–770.
79. Antal SP, Lahey RT Jr, Flaherty JE. Analysis of phase distribution in fully developed laminar bubbly two-phase flow. *Int J Multiphase Flow*. 1991;17:635–652.
80. Lucas D, Krepper E, Prasser HM. Use of models for lift, wall and trubulent dispersion force acting on bubbles for poly-disperse flows. *Chem Eng Sci*. 2007;62:4146–4157.
81. Fu XY, Ishii M. Two-group interfacial area transport in vertical air-water flow I. Mechanistic model. *Nucl Eng Des*. 2002;219:143–168.
82. Fu XY, Ishii M. Two-group interfacial area transport in vertical air-water flow II. Model evaluation. *Nucl Eng Des*. 2002;219:169–190.
83. Sun X, Kim S, Ishii M, Beus SG. Modeling of bubble coalescence and disintegration in confined upward two phase flow. *Nucl Eng Des*. 2004;230:3–26.
84. Sun X, Kim S, Ishii M, Beus SG. Model evaluation of two-group interfacial area transport equation for confined upward flow. *Nucl Eng Des*. 2004;230:27–47.

Manuscript received Oct. 23, 2007, and revision received Feb. 28, 2008.